

Thermal energy census with the Sunyaev-Zel'dovich effect of DESI galaxy clusters/groups and its implication on the weak lensing power spectrum

Ziyang Chen,^{1,2*} Pengjie Zhang,^{1,2,3†} Xiaohu Yang,^{1,2,3}

¹Department of Astronomy, School of Physics and Astronomy, Shanghai Jiao Tong University, Shanghai, 200240, China

²Key Laboratory for Particle Astrophysics and Cosmology (MOE)/Shanghai Key Laboratory for Particle Physics and Cosmology, China

³Tsung-Dao Lee Institute, Shanghai Jiao Tong University, Shanghai 200240, China

Accepted XXX. Received YYY; in original form ZZZ

ABSTRACT

We carry out a thermal energy census of hot baryons at $z < 1$, by cross-correlating the *Planck* MILCA y-map with over 40 DESI galaxy cluster/group subsamples constructed from the Yang et. al (2021) catalog. In our investigation, we select 0.8 million clusters/groups with richness ≥ 5 and estimated halo mass $\geq 10^{13} M_{\odot}/h$. The detection of the thermal Sunyaev-Zel'dovich (tSZ) effect is significant in the investigated clusters/groups. (1) The total measurement S/N of the one-halo term is 65. We constrain the $Y - M$ relation over the halo mass range of $10^{13} - 10^{15} M_{\odot}/h$. We find $Y \propto M^{\alpha}$ with $\alpha = 1.8$ at $z = 0.14$ and $\alpha = 2.1$ at $z = 0.75$. The total thermal energy of gas bound to clusters/groups increases from $0.11 \text{ meV}/\text{cm}^3$ at $z = 0.14$ to $0.23 \text{ meV}/\text{cm}^3$ at $z = 0.75$. (2) The two-halo term measurement constrains the bias-weighted electron pressure $\langle b_y P_e \rangle$. We find that $\langle b_y P_e \rangle$ (in unit of meV/cm^3) increases from 0.25 ± 0.03 at $z = 0.14$ to 0.55 ± 0.04 at $z = 0.75$. These results lead to several implications. (i) The hot gas fraction f_{gas} in clusters/groups monotonically increase with halo mass, where f_{gas} of a $10^{14} M_{\odot}/h$ halo is $\sim 50\%$ (20%) of the cosmic mean at $z = 0.14$ (0.75). (ii) By comparing the 1h- and 2h-terms, we constrain the thermal energy of unbound gas. (iii) The above results lead to a suppression of matter and weak lensing power spectrum. At $l = 10^3$ (10^4), the suppression is $\sim 7\%$ (17%) for source galaxies at $z_s = 1$. These implications are potentially important for gas physics and cosmology, although they suffer from uncertainties in measurements (*Planck* resolution, cluster mass/redshift determination, etc) and gas modeling to be further investigated.

Key words: large-scale-structure; weak lensing;

1 INTRODUCTION

Hot, free electrons in the late universe scatter off CMB photons through the inverse Compton scattering and generate the secondary CMB anisotropies. This is the famous thermal Sunyaev-Zel'dovich (tSZ) effect (Sunyaev & Zeldovich 1972; Carlstrom et al. 2002; Kitayama 2014). It induces a temperature fluctuation ΔT_{tSZ} with a characteristic spectral dependence ($g(x)$) and amplitude described by the Compton y-parameter:

$$\frac{\Delta T_{\text{tSZ}}}{T_{\text{CMB}}} = g(x)y, \quad y = \frac{\sigma_T}{m_e c^2} \int n_e k_B T d\chi. \quad (1)$$

Here $g(x) = x \coth(x/2) - 4$ and $x \equiv hv/k_B T_{\text{CMB}}$.

The tSZ effect contains abundant information of astrophysics and cosmology. In the first, the tSZ effect is a direct probe of cluster pressure profile (Ruppin et al. 2018; Pandey et al. 2021; Ma et al. 2021), baryon abundance (Hernández-Monteagudo et al. 2006; Lim et al. 2018) and distribution (Le Brun et al. 2015; Ma et al. 2015; Kim et al. 2021; Meinke et al. 2021; Amodeo et al. 2021). Even the baryons in filaments can be inferred by stacking

tSZ maps of clusters pairs (Muñoz & Loeb 2018; de Graaff et al. 2019; Tanimura et al. 2019). Also, it can shed light on constraining the strength of supernova and AGN feedback (Hojjati et al. 2017; Spacek et al. 2018; Tröster et al. 2021; Gatti et al. 2021). In addition, the cross-correlation of tSZ with galaxy distribution (Zhang & Pen 2001; Hill et al. 2018; Pandey et al. 2020) or a weak lensing survey (Shao et al. 2011; Hojjati et al. 2015) can increase the measurement significance of tSZ significantly. These kinds of cross-correlation have enabled the measurement of the mean bias-weighted pressure $\langle b_y P_e \rangle$ as a function of redshift (Van Waerbeke et al. 2014; Vikram et al. 2017; Koukoufilippas et al. 2020; Chiang et al. 2020; Yan et al. 2021). Furthermore, the tSZ effect can also constrain cosmological parameters such as σ_8 (Komatsu & Seljak 2002; Horowitz & Seljak 2017; Osato et al. 2020), dark energy properties (Bolliet et al. 2018) and the evolution of T_{CMB} (Hurier et al. 2014).

Direct measurement of cluster tSZ effect by *Planck*, ACT and SPT is limited to clusters with mass $\gtrsim 2 \times 10^{14} M_{\odot}/h$ (Planck Collaboration et al. 2014a; Marriage et al. 2011; Hasselfield et al. 2013; Reichardt et al. 2013; Bleem et al. 2015; Brodwin et al. 2015). Since a large fraction of thermal energy comes from less massive clusters/groups, the above measurements are incapable of carrying out a complete thermal energy census of clusters/groups. On the

* E-mail: chen_zy@sjtu.edu.cn

† E-mail: zhangpj@sjtu.edu.cn

other hand, the cross-correlation measurement with galaxies only measures $\langle b_y P_e \rangle$ and is lack of detailed information on the thermal energy distribution. The recently released group catalog (Yang et al. 2021) provides us a good opportunity to simultaneously measure the thermal energy as a function of cluster mass down to $10^{13} M_\odot/h$ and $\langle b_y P_e \rangle$. This group catalog contains about a million clusters/groups robustly identified (with richness ≥ 5) in the $z < 1$ universe. This data set is not only large in cluster number, but also has reasonable completeness and redshift/mass estimation. It then allows us to detect both the 1h- and 2h-term in the group-tSZ cross-correlation, with high S/N. This measurement will provide valuable information on the thermal energy distribution in the universe, and shed light on important astrophysics such as feedback. It can also put useful constraint on the baryonic effect on weak lensing cosmology.

This paper is organized as follows. We first introduce the data in §2, and then present the method of measuring tSZ in §3. The results are shown and analyzed in §4. We show the implications of this measurement in §5 and finally present our conclusions and discussions in §6. We also include an appendix to explain further details and tests. we adopt a flat cosmology with parameters: $h = 0.676$, $\Omega_{\text{dm}} h^2 = 0.119$, $\Omega_b h^2 = 0.022$, $\sigma_8 = 0.81$ and $n_s = 0.967$ (Planck Collaboration et al. 2020).

2 DATA

2.1 Planck

The *Planck* collaboration released the full-sky Compton parameter map (y-map) of tSZ constructed by two algorithms, NILC and MILCA (Planck Collaboration et al. 2016)¹. These two methods are both based on the Internal Linear Combination (ILC) method and the known spectrum of CMB components. The difference is the method to calculate the optimal scale-independent and spatially-varying linear weight. The performance of NILC and MILCA do not show a distinguishable difference in many studies (Vikram et al. 2017; Koukoufilippas et al. 2020). Besides, a higher noise level is shown in the large-scale of NILC map. Therefore, we choose to utilize the MILCA map to measure y-profile around clusters. Its FWHM is 10 arcmin and nside=2048.

To reduce the contamination from residual Galactic foregrounds, we apply a combination of Planck Galactic mask with 40% sky coverage and a point source mask from the foreground masks used for the Compton parameter analysis provided by *Planck*.

2.2 DESI group catalog

In this work, we use the DESI group catalog obtained by Yang et al. (2021) from the Data Release 9 (DR9) of the DESI Legacy Imaging survey. This group catalog was constructed using an extended version of the halo-based group finder developed by Yang et al. (2005, 2007), which can use photometric or spectroscopic redshifts simultaneously for galaxies. The biggest advantage of this catalog for our concern is that the completeness and purity of clusters with mass larger than $10^{14} M_\odot/h$ is near one. It is well-known that the most of thermal energy of the universe resides in these massive

clusters. The tSZ effect, which is proportional to the thermal energy of baryon, can be detected with high measurement significance with this catalog. Also, this catalog provides an accurate estimation of cluster redshift and mass. The redshift accuracy for groups with more than 10 members is about 0.008. And the uncertainty of halo mass is about 0.2 dex for the massive clusters and about 0.45 dex at the low-mass end.

When measuring the tSZ effect in this work, we only use the clusters with at least 5 members. Because there are relatively large uncertainties in mass and redshift estimation for clusters with $N_g < 5$. And these uncertainties would bias the measurement in an unsuspected way. In addition, the clusters with small richness are usually small-mass halos or even misidentified. Therefore, including them in our measurements, would not improve the S/N significantly.

3 METHOD

To obtain a high significance measurement of the tSZ effect, the secondary anisotropy of CMB, we stack the *Planck* MILCA y-map at the position of galaxy clusters. From DESI group catalog DR9, we can obtain the position, Ra and Dec, of clusters. Then the tSZ plane surrounding each cluster would be cut from the MILCA y-map with the flat approximation. The length of the plane is set to be 160 arcmin and divided into 101×101 grids. The cluster is positioned at the center (origin point) of the plane. Here, we assume the y-profile of a cluster is circular symmetric. So the direction of x, y-axis on the stacking plane can be chosen randomly. Finally, the stacked y-profile around clusters is

$$\hat{y}(\theta_i) = \frac{\sum_j w_j y_j(\vec{\theta})}{\sum_j w_j}, \quad (2)$$

where j represents the j -th cluster in a sample and the length of $\vec{\theta}$ is belong to the i -th θ -bin. To present contamination from Galactic foreground, we adopt the combination of a 40% Galactic Mask and a point source mask both provided by *Planck*. The pixel within the masked region has the weight $w_j = 0$, otherwise $w_j = 1$.

The stacked y-profile $\hat{y}(\theta)$ is the combination of a 1h-term, a 2h-term and a background term coming from residual CMB or other components. Below, we would present how we obtain the template of one- and 2h-terms and how to fit the coefficient of each term.

3.1 1h-term profile

To model the 1h-term of y-profile, we adopt the Komatsu-Seljak (KS) gas density and temperature profiles from Komatsu & Seljak (2001) and follow the simplified version in Mead et al. (2020) with a fixed polytropic index Γ . The model is described in below briefly. The density profile of gravitationally bound gas is

$$\rho_{\text{gas}}(M, r) \propto \left[\frac{\ln(1+r/r_s)}{r/r_s} \right]^{1/(\Gamma-1)}, \quad (3)$$

where $\Gamma = 1.17$ and $r_s = r_v/c$ is the ratio of virial radius and concentration. The concentration-mass relation is

$$c(M) = 7.85 \left(\frac{M}{2 * 10^{12} h^{-1} M_\odot} \right)^{-0.081} (1+z)^{-0.71} \quad (4)$$

(Duffy et al. 2008). Further analysis may adopt more accurate $c - M$ relation, e.g Zhao et al. (2009). The baryon abundance would also

¹ Based on observations obtained with Planck (<http://www.esa.int/Planck>), an ESA science mission with instruments and contributions directly funded by ESA Member States, NASA, and Canada.

influence the concentration of a cluster. And we will discuss this in Appendix.B. The normalization of the above profile is

$$f_{\text{gas}}(M)M = \int_0^{r_v} 4\pi r^2 \rho_{\text{gas}}(M, r) dr. \quad (5)$$

We adopt the fiducial value of $f_{\text{gas}} = \Omega_b/\Omega_m$. The temperature profile is fixed by the hydrostatic equilibrium

$$T_g(M, r) = T_v(M) \frac{\ln(1 + r/r_s)}{r/r_s}, \quad (6)$$

where $T_v(M)$ is the virial temperature

$$\frac{3}{2}k_B T_v(M) = \frac{GMm_p\mu_p}{ar_v}. \quad (7)$$

m_p is the proton mass, μ_p is the mean gas particle mass divided by the proton mass, and a is the scale factor. The electron pressure is the product of density and temperature profile

$$P_e(M, r) = \frac{\rho_{\text{gas}}(M, r)}{m_p\mu_e} k_B T_g(M, r), \quad (8)$$

where $\mu_e = 1.17$ is the mean gas particle mass divided by the proton mass. In the last, the 1h-term y-profile is the integration of $P_e(M, r)$ along the line-of-sight

$$y(\theta) = \frac{\sigma_T}{m_e c^2} \int \frac{d\chi}{1+z} P_e(\chi\theta). \quad (9)$$

The beam size of *Planck* has also been taken into account and approximated using a Gaussian function $W(l) = \exp(-l\sigma_{\text{beam}})^2/2$. For *Planck* MILCA map, $\sigma_{\text{beam}} = \text{FWHM}/2\sqrt{2\ln 2} = 4.25$ arcmin. Therefore, the final 1h-term profile is

$$y_1(\theta) = \int \frac{ldl}{2\pi} J_0(l\theta)y(l)W(l). \quad (10)$$

$y(l)$ is the Hankel transformation of $y(\theta)$

$$y(l) = 2\pi \int J_0(l\theta)y(\theta)\theta d\theta \quad (11)$$

In addition, the mis-centering effect in cluster determination cause a similar effect as the beam. So we replace σ_{beam} as $\sigma_{\text{eff}} \equiv \sqrt{\sigma_{\text{beam}}^2 + \sigma_{\text{mc}}^2}$ to take mis-centering into account

$$\sigma_{\text{mc}} = \eta_{\text{mc}} \frac{r_v}{d_c}, \quad (12)$$

r_v and d_c are the virial radius and comoving distance of a cluster. The default value of η_{mc} is set to 0.2. We will discuss how this parameter would influence the results in Appendix.C

3.2 2h-term profile

The 2h-term would also contribute to the stacked y-profile $\hat{y}(\theta)$. Its profile is proportional to

$$\frac{\sigma_T}{(1+z)m_e c^2} \int \xi_{mm}(r_{\perp} = \chi\theta, r_{\parallel}|z_g) dr_{\parallel}. \quad (13)$$

The integration of the correlation function is

$$\int \xi_{mm}(r_{\perp}, r_{\parallel}|z_g) dr_{\parallel} = \int P_m(k = k_{\perp}, z) e^{ik_{\perp}r_{\perp} \cos \phi} \frac{k_{\perp} dk_{\perp} d\phi}{(2\pi)^2}, \quad (14)$$

$P_m(k, z)$ is the matter power spectrum at redshift z . Since

$$\int_0^{2\pi} e^{ik_{\perp}r_{\perp} \cos \phi} = 2\pi J_0(k_{\perp}r_{\perp}), \quad (15)$$

and the template of 2h-term profile is

$$y_2(\theta) = \int P_m(k = k_{\perp}, z) e^{-\frac{k_{\perp}^2 \sigma_{\text{beam}}^2 d_c^2(z)}{2}} J_0(k_{\perp}r_{\perp}) \frac{k_{\perp} dk_{\perp}}{2\pi} \quad (16)$$

Here, we consider the smoothing effect from beam size of CMB survey.

3.3 Fitting

We assume the measured stacking tSZ profile contains three components and the theoretical model is

$$y^{\text{th}}(\theta) = A_1 y_1(\theta) + A_2 y_2(\theta) + A_3 y_3(\theta). \quad (17)$$

A_1 is the coefficient of the 1h-term profile within our methodology. Its physical meaning is the ratio of the fraction of gas in a cluster and the mean fraction of baryon in the universe.

$$A_1 = \frac{f_{\text{gas}}}{\Omega_b/\Omega_m}. \quad (18)$$

A_2 is the coefficient of the 2h-term

$$A_2 = \langle b_g b_y P_e \rangle. \quad (19)$$

In addition, $y_3(\theta) = \mathbf{1}$ represents a scale-independent background term, in order to consider residuals of other CMB components which would contaminate the MILCA y-map.

From Eq.10 and 16, the 1h-term template $y_1(\theta)$ relies on the mass and redshift distribution of the stacked cluster sample, while the 2h-template $y_2(\theta)$ only relies on the redshift distribution. It is worth noting that the mass estimated in DESI group catalog DR9 is higher than the true value and the uncertainty is about 0.2 to 0.45 dex from high-mass to low-mass end (as shown in Fig.9 in Yang et al. (2021)). We discuss in Appendix.A about how to obtain an unbiased 1h-term estimation.

To obtain the best-fit value of A_1 , A_2 and A_3 , we minimize the likelihood

$$-\ln L = \frac{1}{2} \chi^2, \quad (20)$$

and

$$\chi^2 = [\hat{y}(\vec{\theta}) - y^{\text{th}}(\vec{\theta})]^{\dagger} \mathbf{C}^{-1} [\hat{y}(\vec{\theta}) - y^{\text{th}}(\vec{\theta})].$$

\mathbf{C} is the covariance matrix. We estimate it by Jackknife resampling. The number of the Jackknife sample is set to be $N_{\text{JK}} = 100$. The Fisher matrix is

$$\mathbf{F} = \begin{pmatrix} \mathbf{y}_1^T \mathbf{C}^{-1} \mathbf{y}_1 & \mathbf{y}_1^T \mathbf{C}^{-1} \mathbf{y}_2 & \mathbf{y}_1^T \mathbf{C}^{-1} \mathbf{y}_3 \\ \mathbf{y}_2^T \mathbf{C}^{-1} \mathbf{y}_1 & \mathbf{y}_2^T \mathbf{C}^{-1} \mathbf{y}_2 & \mathbf{y}_2^T \mathbf{C}^{-1} \mathbf{y}_3 \\ \mathbf{y}_3^T \mathbf{C}^{-1} \mathbf{y}_1 & \mathbf{y}_3^T \mathbf{C}^{-1} \mathbf{y}_2 & \mathbf{y}_3^T \mathbf{C}^{-1} \mathbf{y}_3 \end{pmatrix}, \quad (21)$$

where

$$\mathbf{y}_i = (y_i(\theta_1), y_i(\theta_2), \dots, y_i(\theta_n))^T \quad (22)$$

is the template of 1h-, 2h-term or background term. The best-fitting values of A_1 , A_2 and A_3 are the solution of equation

$$\mathbf{F} \times \begin{pmatrix} A_1 \\ A_2 \\ A_3 \end{pmatrix} = \begin{pmatrix} \mathbf{y}_1 \mathbf{C}^{-1} \hat{y} \\ \mathbf{y}_2 \mathbf{C}^{-1} \hat{y} \\ \mathbf{y}_3 \mathbf{C}^{-1} \hat{y} \end{pmatrix} \quad (23)$$

And the uncertainty of A_i is

$$\sigma_i^2 = (\mathbf{F}^{-1})_{ii}. \quad (24)$$

range of z	range of $\lg M_L$	N_{cluster}	$\lg M_t$	\bar{b}_g	A_1	S/N(A_1)	A_2	S/N(A_2)	$A_3 \times 10^8$	S/N(A_3)	χ_{min}^2
[0.0, 0.2)	[14.7, 15.5)	228	14.67	4.41	0.66	8.2	1.59	1.1	1.02	0.1	2.73
[0.0, 0.2)	[14.5, 14.7)	470	14.45	3.36	0.658	10.55	2.2	1.7	-6.43	1.0	0.82
[0.0, 0.2)	[14.3, 14.5)	1054	14.31	2.92	0.483	11.11	0.87	1.8	-2.08	0.7	1.26
[0.0, 0.2)	[14.1, 14.3)	1557	14.11	2.58	0.477	8.45	1.01	2.9	-2.97	1.6	3.33
[0.0, 0.2)	[13.9, 14.1)	3744	13.9	2.18	0.496	8.66	0.77	4.4	-1.71	1.5	5.66
[0.0, 0.2)	[13.5, 13.9)	16970	13.59	1.79	0.449	6.78	0.48	5.1	-1.03	1.8	2.77
[0.0, 0.2)	[13, 13.5)	58072	13.16	1.4	0.387	2.4	0.25	4.8	0.01	0.0	4.85
[0.0, 0.2)	[12, 13)	67824	12.65	1.14	1.694	2.59	0.49	11.2	-1.49	4.7	10.92
[0.2, 0.4)	[14.9, 15.5)	266	14.86	6.02	0.516	13.96	-0.69	0.5	2.32	0.5	13.79
[0.2, 0.4)	[14.8, 14.9)	368	14.68	4.91	0.575	11.39	0.87	0.9	3.78	1.0	1.78
[0.2, 0.4)	[14.7, 14.8)	566	14.58	4.41	0.524	14.45	1.72	2.8	-3.06	1.5	4.75
[0.2, 0.4)	[14.6, 14.7)	897	14.51	3.97	0.494	15.8	1.15	2.1	-2.83	1.5	9.33
[0.2, 0.4)	[14.5, 14.6)	1538	14.41	3.63	0.507	17.69	1.08	2.6	-1.75	1.3	2.38
[0.2, 0.4)	[14.4, 14.5)	2748	14.37	3.4	0.372	14.98	0.74	2.4	0.93	0.9	4.25
[0.2, 0.4)	[14.3, 14.4)	4030	14.26	3.21	0.332	11.68	1.15	4.6	-0.82	0.9	6.15
[0.2, 0.4)	[14.2, 14.3)	5273	14.16	3.02	0.336	10.38	0.67	3.0	-0.28	0.4	10.2
[0.2, 0.4)	[14, 14.2)	18353	14.0	2.63	0.352	12.59	0.73	5.4	-0.01	0.0	1.25
[0.2, 0.4)	[13.7, 14)	67475	13.74	2.18	0.275	6.45	0.5	8.4	-0.18	0.8	5.23
[0.2, 0.4)	[13.4, 13.7)	142527	13.46	1.84	0.323	4.11	0.43	9.4	0.14	0.9	6.6
[0.2, 0.4)	[13, 13.4)	248157	13.14	1.52	0.396	2.43	0.47	15.0	-0.07	0.6	7.95
[0.2, 0.4)	[11, 13)	111593	12.75	1.26	5.915	5.8	0.57	13.6	-0.65	4.2	24.08
[0.4, 0.6)	[14.9, 15.5)	204	14.85	6.93	0.459	9.16	3.45	1.8	-0.22	0.1	8.84
[0.4, 0.6)	[14.8, 14.9)	267	14.68	5.74	0.521	12.82	2.12	1.3	2.9	1.1	5.89
[0.4, 0.6)	[14.7, 14.8)	454	14.58	5.14	0.559	13.35	1.52	1.3	-0.8	0.4	1.79
[0.4, 0.6)	[14.6, 14.7)	757	14.51	4.64	0.507	11.34	3.63	4.2	-0.46	0.3	5.79
[0.4, 0.6)	[14.5, 14.6)	1692	14.41	4.23	0.545	14.95	1.56	2.4	0.14	0.1	1.62
[0.4, 0.6)	[14.4, 14.5)	3648	14.36	3.95	0.354	12.43	2.21	4.4	0.38	0.4	6.7
[0.4, 0.6)	[14.3, 14.4)	4772	14.27	3.74	0.358	11.38	1.43	3.4	0.57	0.8	3.84
[0.4, 0.6)	[14.2, 14.3)	7901	14.16	3.48	0.3	7.53	1.78	6.7	-0.54	1.0	9.71
[0.4, 0.6)	[14, 14.2)	25281	14.01	3.07	0.297	8.09	1.33	7.0	0.24	0.8	7.16
[0.4, 0.6)	[13.7, 14)	98374	13.74	2.5	0.179	3.99	0.96	12.6	0.28	1.8	17.53
[0.4, 0.6)	[13.4, 13.7)	232071	13.46	2.07	0.151	1.66	0.61	10.7	0.63	6.2	3.81
[0.4, 0.6)	[13, 13.4)	214509	13.16	1.7	0.232	0.9	0.54	10.7	0.79	7.5	7.23
[0.4, 0.6)	[11, 13)	33964	12.8	1.4	5.68	2.5	0.58	4.9	1.18	4.6	15.54
[0.6, 1.0)	[14.7, 15.5)	459	14.64	6.85	0.507	11.06	3.53	1.5	1.2	0.6	0.78
[0.6, 1.0)	[14.6, 14.7)	689	14.51	5.66	0.397	8.28	4.44	2.7	-3.35	2.1	2.05
[0.6, 1.0)	[14.5, 14.6)	1834	14.41	5.16	0.357	10.38	3.48	3.6	0.1	0.1	8.59
[0.6, 1.0)	[14.4, 14.5)	3237	14.36	4.79	0.294	10.03	3.51	4.5	0.19	0.2	2.68
[0.6, 1.0)	[14.3, 14.4)	5657	14.26	4.58	0.327	9.96	2.15	3.2	0.45	0.7	1.75
[0.6, 1.0)	[14.2, 14.3)	11650	14.16	4.29	0.235	6.77	2.98	6.5	-0.03	0.1	6.65
[0.6, 1.0)	[14.1, 14.2)	15669	14.06	3.88	0.27	8.16	1.61	4.8	0.99	2.7	6.2
[0.6, 1.0)	[13.5, 14.1)	189946	13.73	2.99	0.23	6.31	1.14	12.1	0.48	4.0	6.65
[0.6, 1.0)	[13, 13.5)	19256	13.32	2.07	-0.715	1.37	0.62	2.5	0.46	1.6	1.18

Table 1. The detailed information of tSZ stacking measurement and fitting in different mass and redshift bins. The first and second columns are the redshift and mass range of clusters in each bin. The third column is the number of clusters. The fourth and fifth column is the mean calibrated mass and galaxy bias. The 6th and 7th columns are the best-fitted value and S/N of the coefficient for the 1h-term. The 8th to 11th columns are those for the 2h-term and the background term. The last column is the χ_{min}^2 for fitting in this bin. The number of data points at each bin is 40. But due to strong correlation between adjacent data points, the number of independent data points is ~ 10 . Given 3 fitting parameters, $\chi_{\text{min}}^2 \lesssim 10$ is reasonable. The bins with $M_L < 10^{13} M_{\odot}/h$ are not used to measure the $Y - M$, $f_{\text{gas}} - M$ relation and $\langle b_y P_e \rangle$ due to relatively high χ_{min}^2 and significant detection of the background term.

4 RESULT ANALYSIS

We measure the stacked tSZ profile from *Planck* MILCA map and DESI group catalog DR9. To investigate how the tSZ effect would depend on the cluster mass and redshift, we divide the cluster sample into several redshift and mass bins. In the first we have 4 redshift bins: $0 \leq z < 0.2$, $0.2 \leq z < 0.4$, $0.4 \leq z < 0.6$ and $0.6 \leq z \leq 1$. Then, the binning strategy for cluster mass is to keep the balance between making the measurement significant and increasing the bin number to capture the shape of $f_{\text{gas}}(M)$. In total

we have more than 40 cluster/group subsamples.

The stacked tSZ profiles as a function of angular radius are shown in Fig.1. For brevity, we only show the results of $0.4 \leq z < 0.6$. The results of the other three redshift bins are similar. As expected, the stacked tSZ peaks at the center and decreases with increasing radius. The peak value drops nearly monotonically with decreasing cluster mass. It drops by a factor of 50 from the most massive cluster ($10^{15} M_{\odot}/h$) to small groups ($10^{11} \sim 10^{13} M_{\odot}/h$).

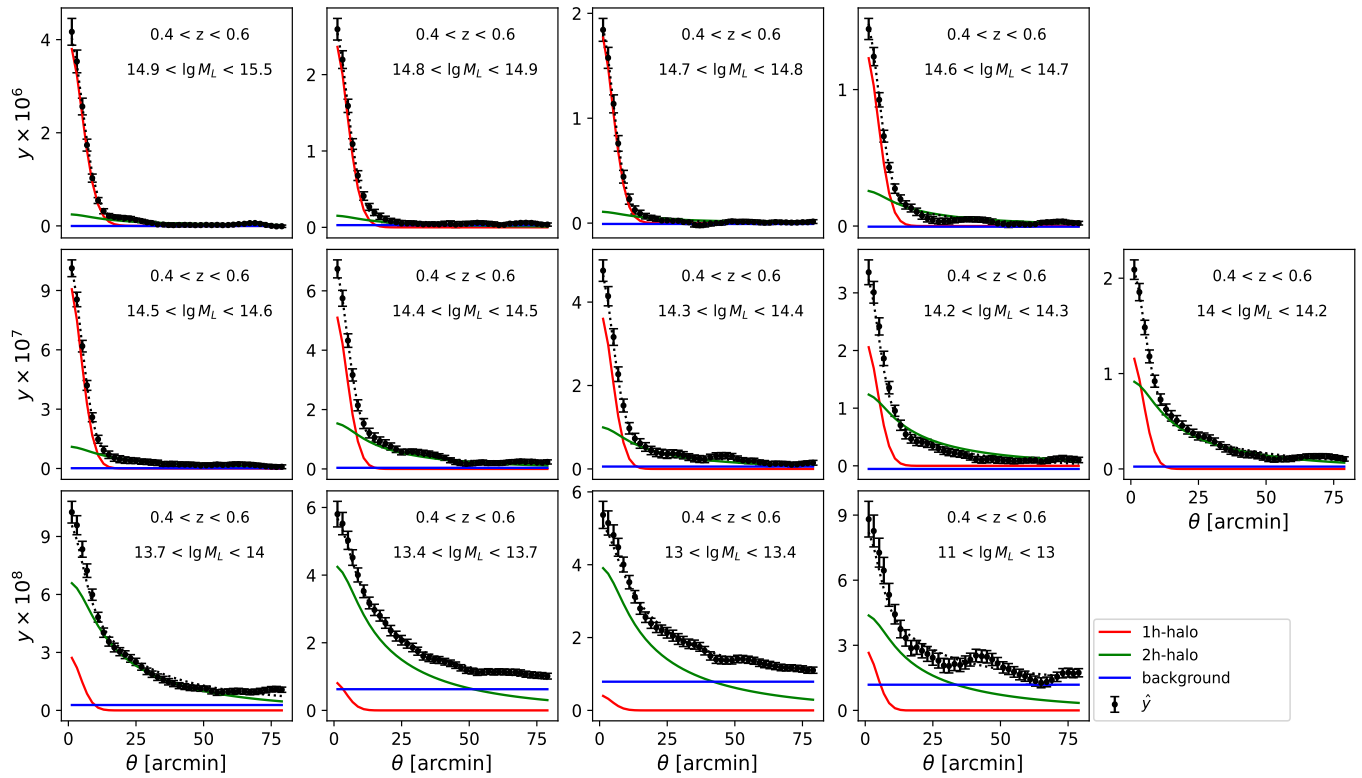


Figure 1. The stacking results of tSZ measurements as a function of angular distance to the center of clusters. Each panel shows the result of a mass bin with $0.4 \leq z < 0.6$. The black dots are the stacking results with errorbars estimated by Jackknife resampling. The red, green and blue lines represent the bestfit one-halo, 2h-and the background term. The dotted lines are the sum of these three terms.

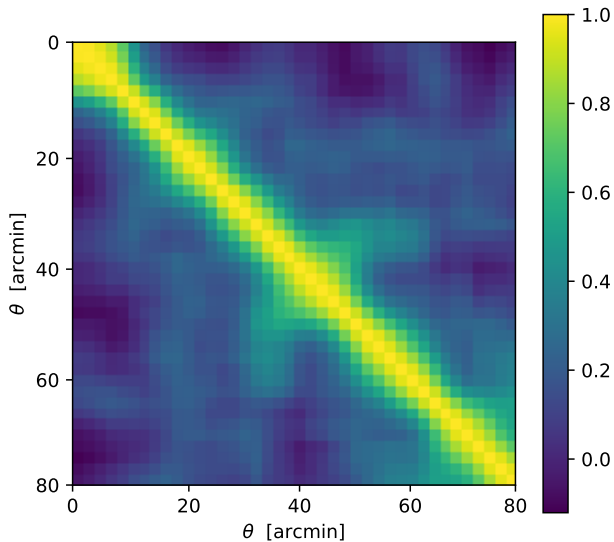


Figure 2. The normalized covariance matrix of data points shown in Fig.1. Here we only show the result of a cluster sample with $0.4 \leq z < 0.6$ and $14.9 < \lg M_L < 15.5$ (top left panel in Fig.1). The covariance matrices for other cluster samples are similar. Near data points are strongly correlated, largely due to the *Planck* beam.

Fig.2 shows the normalized covariance matrix for the most massive bin in $0.4 \leq z < 0.6$. The covariance of other bins is similar. There is large correlation between neighboring bins separated by $\lesssim 5$ arcmin. This may be caused by the beam and mis-centering effect which mix the signal at different radius scale. So despite the fact that we have 40 data points for each sample, the really degree of freedom (namely independent data points) is ~ 10 . For these reason, we choose $\chi^2_{\min} \leq 10$ as the criterion of a good fit.

The combination of a 1h-term template (Eq.10), a 2h-term template (Eq.16) and a constant background term are fitted to the measured tSZ signal. The fitted A_i and their uncertainties are shown in Table.1. When the cluster mass is larger than $10^{14.5} M_\odot/h$, the 1h-term dominates the y-profile and the measurement significance of the 1h-term is high. When $M \leq 10^{13} M_\odot/h$, the amplitude of the background is comparable to that of the 1h- and 2h-terms. At this mass range, the shape of the background becomes important. The large fluctuations at $\theta > 20$ arcmin in the mass bin $10^{11} M_\odot/h < M_L < 10^{13} M_\odot/h$ may indicate a radius-dependent background.

We exclude the cluster samples with both (1) $\chi^2_{\min} \geq 10$ and (2) $S/N(A_3) \geq 4$. A cluster sample with $S/N(A_3) \geq 4$ but $\chi^2_{\min} < 10$ means a significant detection of a residual background term, but our model is still a good description of the data. On the other hand, a cluster sample with $S/N(A_3) < 4$ but $\chi^2_{\min} \geq 10$ means a poor fit but it is the modeling of tSZ to be improved. For these reasons, we only excluded the cluster samples satisfying both criteria. Therefore,

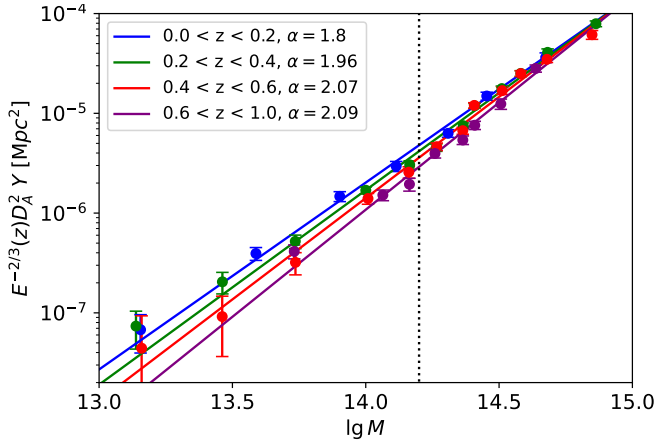


Figure 3. The relation between parameter Y (Eq.25) and cluster mass M . The points with errorbars represent measurement results from 1h-term. These points can be described by Eq.28 shown as solid lines. α is the slope in the relation Eq.26. The dash vertical line represents a typical lower mass limit in previous X-ray or SZ cluster samples. Since the data now spans two orders of magnitude in M , constraints on alpha are tight.

all samples with $M_L < 10^{13} M_\odot/h$ are excluded.

4.1 1h-term measurement

The 1h-term of tSZ profile is determined by thermal energy distribution in a halo. We utilize its measurement to constrain $Y - M$ relation and find this relation is redshift-dependent. Then we conduct a thermal energy census by integrating all thermal energy in halos of the whole mass range.

4.1.1 $Y - M$ relation

With the measurement of 1h-term coefficient A_1 and template $y_1(\theta)$ (Eq.10), we calculate the parameter Y ²

$$Y = \int A_1 y_1(\theta) d^2\theta \quad (25)$$

as a function of cluster mass in different redshift bins. The $Y - M$ relation is shown in Fig.3 and fitted with

$$Y \propto M^\alpha. \quad (26)$$

Under the hydrostatic equilibrium, the slope $\alpha = 5/3$. In our measurement the slope is larger than 1.8 and slightly increases with redshift.

$$\alpha = 1.81 + 0.45z. \quad (27)$$

Over the last decade, a significant size of SZ-selected samples have been published by *Planck* (Planck Collaboration et al. 2014b,a, 2015), ACT (Marriage et al. 2011; Hasselfield et al. 2013), SPT (Reichardt et al. 2013; Bleem et al. 2015) and other surveys (Brodwin et al. 2015). Our work probes the $Y - M$ relation down to much lower mass ($10^{13} M_\odot/h \sim 10^{14} M_\odot/h$) than the above samples. Adopted

² $y_1(\theta)$ here induces the beam effect, so the integral is $0 < \theta < \infty$. This equals to the integral of the original $y_1(\theta)$ to θ_{vir}

the formula in (Planck Collaboration et al. 2014b), we find the $Y - M$ relation can be described by

$$E^{-3/2}(z) \left[\frac{D_A^2 Y}{10^{-3.84} \text{Mpc}^2} \right] = \left(\frac{M}{10^{15} M_\odot/h} \right)^{1.81+0.45z}, \quad (28)$$

which shown as the solid lines in Fig.3. Here,

$$E(z) = \sqrt{\Omega_m(1+z)^3 + \Omega_\Lambda} \quad (29)$$

assuming the universe is flat and D_A is the angular distance. We assume only the slope is dependent on redshift.

4.1.2 Thermal energy census of bound gas

The thermal energy of baryons, although tiny, is an important property of the universe (Fukugita & Peebles 2004; Zhang et al. 2004; Chiang et al. 2020). The tSZ effect is contributed by all thermal energy in the universe. It is known that most thermal energy resides in the center of massive clusters, which is also observed in IllustrisTNG simulation (Gouin et al. 2022). Thanks to the high completeness of DESI group catalog DR9 which contains almost all massive clusters from $z=0$ to $z=1$, a census of thermal energy which bound to halos in the universe can be conducted. The relation between thermal gas pressure and the electron pressure measured by the tSZ effect is

$$P_{\text{th}} = \frac{3 + 5X}{2 + 2X} P_e, \quad (30)$$

where $X=0.76$ is the primordial hydrogen abundance, P_e is from Eq.8 and $f_{\text{gas}} = A_1 \Omega_b / \Omega_m$ obtained by 1h-term measurement. With the assumption that baryons are fully ionized, $P_{\text{th}} = 1.93 P_e$. And the thermal energy

$$E_{\text{th}} = \frac{3}{2} P_{\text{th}}. \quad (31)$$

Therefore the total thermal energy density bound to halos is

$$E = \int \left(\int E_{\text{th}} dV \right) \frac{dn}{d \lg M} d \lg M. \quad (32)$$

The inner integration represents the total thermal energy in a halo with mass M .

In Fig.4, the dashed lines show the contribution of thermal energy from clusters with different masses. Most of the thermal energy is coming from clusters with mass ranging from $10^{14} M_\odot/h$ to $10^{15} M_\odot/h$. A half of thermal energy is coming from cluster whose mass is above $10^{14.46}, 10^{14.51}, 10^{14.46}, 10^{14.12} M_\odot/h$ in redshift bin $0 \leq z < 0.2, 0.2 \leq z < 0.4, 0.4 \leq z < 0.6, 0.6 \leq z \leq 1$. And the peak tends to move to lower mass with the increasing of redshift. And solid lines show the accumulated thermal energy as a function of cluster mass. A plateau is reached before $M = 10^{12} M_\odot/h$ in all redshift bins, which means the thermal energy in cluster with mass small than $10^{12} M_\odot/h$ can be ignored. In our measurement, the thermal energy bound to halos is $0.1076 \pm 0.0031, 0.1877 \pm 0.0044, 0.2003 \pm 0.0019$ and 0.2314 ± 0.0019 [meV/cm³] in redshift bin $0 \leq z < 0.2, 0.2 \leq z < 0.4, 0.4 \leq z < 0.6$ and $0.6 \leq z \leq 1$.

4.2 2h-term measurement: $\langle b_y P_e \rangle$

The coefficient of the 2h-term A_2 is the product of the galaxy bias $\langle b_g \rangle$ (listed in Table.1) and the bias-weighted electron pressure $\langle b_y P_e \rangle$. We estimate $\langle b_y \rangle$ from the distribution of $\lg M_i$ of the cluster

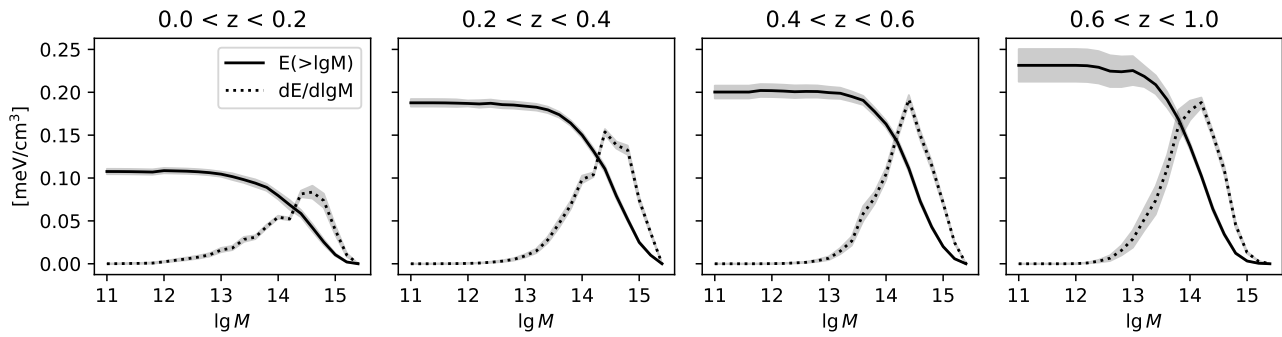


Figure 4. The thermal energy census of hot baryons bound to clusters/groups. The dashed lines show the thermal energy contributed by halos with different mass. The solid lines show the accumulative thermal energy. The grey shadow region is the uncertainty from the estimation of $\lg M_0$ and β in $f_{\text{gas}} - \lg M$ relation.

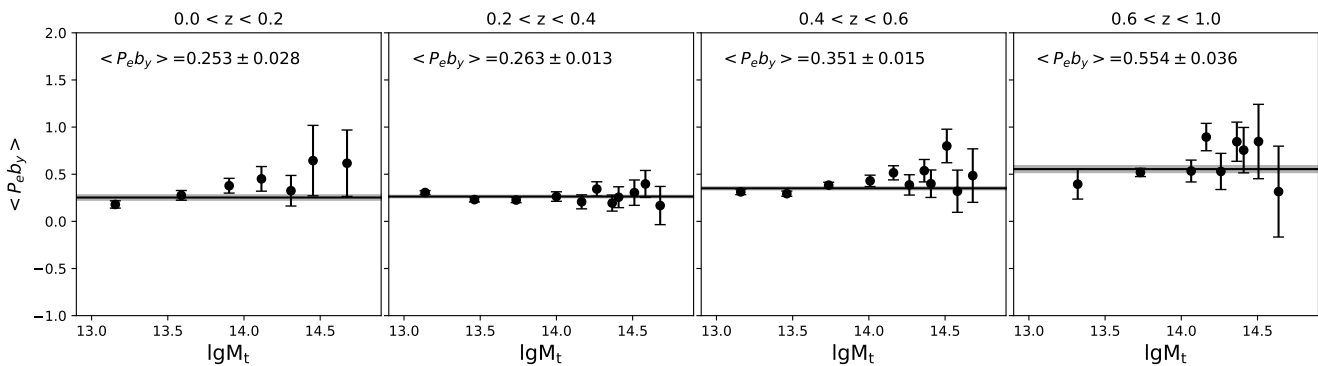


Figure 5. The bias-weighted electron pressure $\langle b_y P_e \rangle$ as a function of the calibrated cluster/group mass in four redshift bins. The solid line is the mean value estimated from all mass bins in this redshift (Eq.33) and the grey shadow region is the corresponding uncertainty. These two are labeled on the top left of each panel.

range of z	z_{mean}	$\langle b_y P_e \rangle$ [meV/cm^3]
[0.0, 0.2)	0.14	0.253 ± 0.028
[0.2, 0.4)	0.31	0.263 ± 0.013
[0.4, 0.6)	0.49	0.351 ± 0.015
[0.6, 1.0)	0.75	0.554 ± 0.036
[0.1, 0.2)	0.15	0.196 ± 0.025
[0.2, 0.3)	0.25	0.219 ± 0.017
[0.3, 0.4)	0.35	0.291 ± 0.018
[0.4, 0.5)	0.45	0.297 ± 0.018
[0.5, 0.6)	0.55	0.414 ± 0.028

Table 2. The best-fitted value of the bias-weighted electron pressure and its uncertainty of each redshift bin.

sample and the bias-mass relation (Sheth et al. 2001). Then we show $\langle b_y P_e \rangle = A_2 / \langle b_g \rangle$ of different mass and redshift bins in Fig.5. The value of different mass bins in the same redshift bin are consistent with each other in the 1σ -errorbar. This means A_2 is proportional to galaxy bias $\langle b_g \rangle$, as expected. The $\langle b_y P_e \rangle$ estimated from all mass bins is

$$\langle b_y P_e \rangle = \frac{\sum_i \langle b_y P_e \rangle_i / \sigma_i^2}{\sum_i 1 / \sigma_i^2}, \quad (33)$$

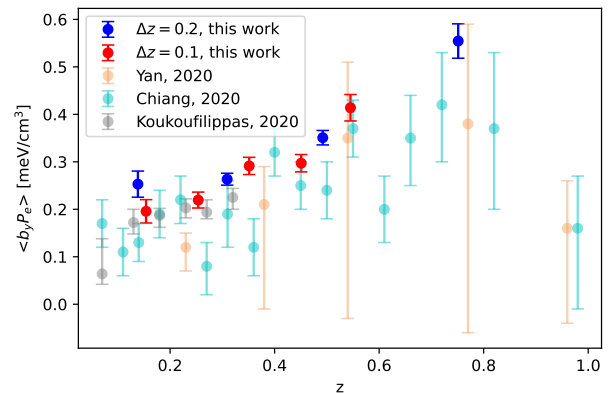


Figure 6. The comparison of $\langle b_y P_e \rangle$ with other literature. The blue and red points are our measurements with $\Delta z = 0.2$ and $\Delta z = 0.1$. The orange, cyan and grey points are the measurements from Yan et al. (2021); Chiang et al. (2020); Koukoufilippas et al. (2020). All these data points measured by different methods and data sets are consistent.

where i represents different mass bins in the same redshift bin.

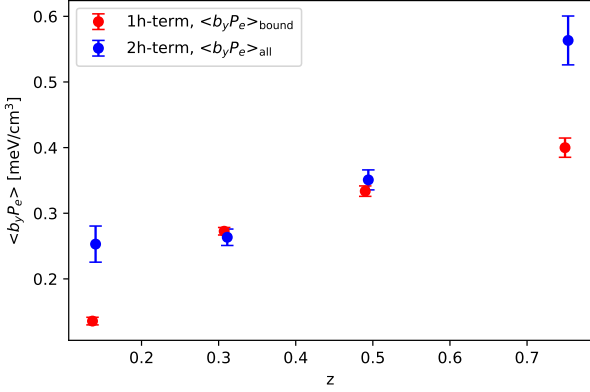


Figure 7. The comparison of $\langle b_y P_e \rangle$ induced from 1h- and 2h-terms. This plot verifies the consistency relation Eq.37.

The measured bias-weighted electron pressure as a function of redshift is shown in Fig.6. $\langle b_y P_e \rangle$ increases monotonically with increasing redshift. The redshift interval is $\Delta z = 0.2$ in our fiducial measurement. We find that $\langle b_y P_e \rangle$ increases significantly with z . Therefore we also try a finer redshift bin size $\Delta z = 0.1$. The uncertainty of each red point is larger than that of each blue point due to the decreasing number of clusters in a narrow redshift bin. Besides, the measurements of different redshift bin lengths are consistent with each other. The measurements of these redshift bins are summarized in Table.2.

We also show the comparison with other measurements in literature. Yan et al. (2021) adopts the galaxy-tSZ-CMB lensing cross-correlation using *Planck* and KiDS data. Chiang et al. (2020) uses the tomographic tSZ measurements from the *Planck* and a spectroscopic galaxy sample from SDSS. Koukoufilippas et al. (2020) uses the same method but a photometric redshift galaxy sample from WISE \times SuperCOSMOS public catalog (grey points). In Fig.6, these results from different methods and different data sets are consistent with each other.

4.3 Consistency of 1h- and 2h-terms

From the measurement of 1h-term, the electron pressure density profile $P_e(r)$ of a halo with a given mass and redshift can be inferred. TSZ 2h-term (Sec.4.2) measures the mean $\langle b_y P_e \rangle$ as a function of redshift. In this subsection, we check the consistency between the 1h- and 2h-term measurements. With the assumption of the halo model, the mean electron pressure which is bound to halos is

$$\langle P_e \rangle_{\text{bound}} = \int \left(\int P_e dV \right) \frac{dn}{dM} dM, \quad (34)$$

and

$$b_{y,\text{bound}} = \frac{\int b_g \bar{y} \frac{dn}{dM} dM}{\int b_g \frac{dn}{dM} dM}. \quad (35)$$

We adopt the halo mass function and bias-mass relation from (Sheth et al. 2001). Then we estimated the $\langle b_y P_e \rangle_{\text{bound}}$ from 1h-term measurement. The comparison with the measurement from 2h-term is shown in Fig.7. $\langle b_y P_e \rangle$ measured by the two halo term is the sum of

that of bound and unbound gas

$$\langle b_y P_e \rangle = \langle b_y P_e \rangle_{\text{bound}} + \langle b_y P_e \rangle_{\text{unbound}}. \quad (36)$$

Therefore,

$$\langle b_y P_e \rangle > \langle b_y P_e \rangle_{\text{bound}}. \quad (37)$$

Eq.37 is the consistency relation that we need to test with the both 1h- and 2h-term measurements. Fig.7 shows that this relation is indeed satisfied at all four redshift bins. We will further discuss the difference between $\langle b_y P_e \rangle$ and $\langle b_y P_e \rangle_{\text{bound}}$ in Sec.5.2.

5 ASTROPHYSICAL AND COSMOLOGICAL IMPLICATIONS

5.1 Baryon abundance in clusters

The baryon feedback, such as SN and AGN, would heat/blow the gas out of the halo. The potential suppression of gas fraction is captured by the parameter A_1 .³ Given A_1 measurement in Table.1, we obtain the relationship between A_1 and the cluster mass M_t at each redshift. We fit this relation against the formula (Schneider & Teyssier 2015)

$$A_1 = \frac{f_{\text{gas}}}{\Omega_b/\Omega_m} = \frac{(M/M_0)^\beta}{1 + (M/M_0)^\beta}, \quad (38)$$

where $\lg M_0$ and β are the parameters to fit. In this parameterization, the gas fraction of a cluster with $M = M_0$ is 50% of the cosmic mean.

The fitting results are shown in Fig.8. We discard the the most massive bin of $0.2 \leq z < 0.4$ and $0.4 \leq z < 0.6$, because their mass distribution may be modeled inaccurately (Appendix.A). The best-fitting values and the uncertainties of $\lg M_0$ and β are also shown in Fig.8.

The baryon abundance becomes lower as the decreasing of the halo mass in each redshift bin. $M_0 = 10^{14.05, 14.65, 14.61, 14.82} M_\odot/h$ at redshift bin $0 \leq z < 0.2$, $0.2 \leq z < 0.4$, $0.4 \leq z < 0.6$ and $0.6 \leq z \leq 1$. Correspondingly, $\beta = 0.18 \pm 0.14, 0.44 \pm 0.07, 0.64 \pm 0.09, 0.57 \pm 0.13$. These results imply a strong impact of feedback on cluster gas fraction. In addition, we find a slight evolution of cluster baryon abundance with redshift. The baryon abundance is higher in low redshift than high redshift in halos with the same mass. We will verify these findings in a future work, especially with the help of hydroynamical simulations.

In previous works, halo baryon abundance is usually measured by X-ray observation. Sun et al. (2009) finds a average value $f_{\text{gas}} \sim 0.12$ and the slope of $f_{\text{gas}} - M_{500}$ relation is 0.135 ± 0.030 with large scatter, using 43 nearby galaxy groups with $10^{13} < M_{500} < 10^{14} M_\odot/h$, $0.012 < z < 0.12$ based on *Chandra* archival data. With 49 low-redshift clusters provided by *Chandra* and ROSTA data, Vikhlinin et al. (2009) fits a linear relation of f_{gas} and $\lg M_{500}$ with the mass range $M_{500} > 13.7 M_\odot/h$. In addition, Gonzalez et al. (2013) finds a $f_{\text{gas}} - M_{500}$ relation $f_{\text{gas}} \propto M_{500}^{0.26 \pm 0.03}$ for 12 galaxy groups/clusters at $z \sim 0.1$

³ This interpretation of A_1 relies on the condition that the modeling of $y_1(\theta)$ is accurate. To be specific, the validity of the A_1 interpretation assumes that feedback would not change the temperature profile. This assumption is valid at the first order in which the temperature is fixed by the gravitational potential. But at high order, this interpretation may be inaccurate.

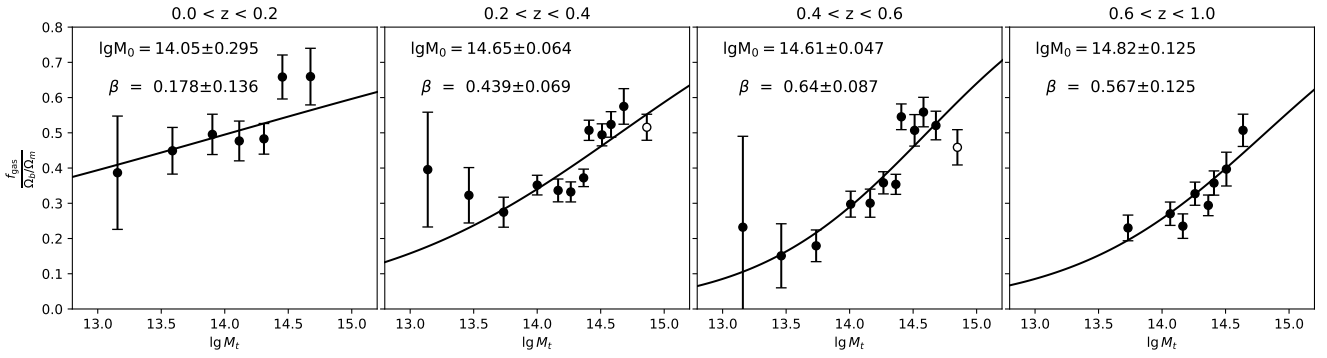


Figure 8. The gas abundance as a function of cluster mass in four redshift bins. In each panel, the black points are the fitting coefficients of the 1h-term template. The solid line is the fitting of Eq.38 with these black points, while the hollow circle points are not included in the fitting. The best-fitting values and uncertainties of the parameters $\lg M_0$ and β are shown on the top-left corner of the panel.

with $10^{14} < M_{500} < 5 \times 10^{14} M_{\odot}/h$ observed by *XMM-Newton* X-ray telescope. There is distinguishable difference in slope for cluster samples with different mass range. Utilizing all above X-ray measurements, [Schneider & Teyssier \(2015\)](#) parametrise the $f_{\text{gas}} - M_{500}$ relation as Eq. 38 with the best-fitting parameters $M_0 = 1.2 \times 10^{14} M_{\odot}/h$ and $\beta = 0.6$. $\beta = 0.6$ is different from our measurement $\beta = 0.178 \pm 0.136$ in $0 \leq z < 0.2$. This may be caused by the poor description of the measurement by Eq. 38 (left panel in Fig. 8). Considering the large measurement uncertainty and different mass definition, however, these X-ray measurements are consistent with our results in the lowest redshift bin. Also, [Lim et al. \(2018\)](#) constrains the hot gas fraction using tSZ effect with the combination of *Planck* and a group catalog given in [Lim et al. \(2017\)](#) at redshift $z < 0.2$. Although they only adopt low redshift cluster samples, when $M_{200} > 10^{13.5} M_{\odot}/h$ they find a similar relation with ours.

In addition, we caution that the above obtained gas fraction in dark matter halos, f_{gas} , depends on our model assumption of the hydrostatic equilibrium of gas temperature (e.g., Eq. 6), and in general it can be regarded as the ‘hot’ gas fraction. In case that the gas temperature is much lower than the virial temperature of the dark matter halos, the f_{gas} will be underestimated. Very interestingly, in a recent paper, using the kSZ effect around 40000 low redshift groups in the SDSS observation, [Lim et al. \(2020\)](#) claimed the detection of the ‘missing baryons’. The total kSZE flux within halos estimated implies that the gas fraction in halos is about the universal baryon fraction, even in low-mass halos with mass $\sim 10^{12.5} M_{\odot}/h$. It thus indicates that the gas temperature is indeed significantly lower than the halo virial temperature.

5.2 Pressure from unbound gas

When the gas is ejected from the halo, its distribution and phase can hardly be measured. The feedback process injects thermal or kinematic energy into these gas. They may lose the energy when escaping from the gravitational wall of the halo or still stay hot. Some models treat these gas just as a diffuse background and only contribute to the 2h-term. And some other models think these gas would not be flowed too far away from the halo and reside around the halo, as the so-called Circum-Galactic Medium (CGM). Due to the low density of these unbound gas, the measurement of them is very difficult.

range of z	$\langle b_y P_e \rangle_{\text{unbound}} [meV/cm^3]$	scenario 1	scenario2
[0.0, 0.2)	0.117 ± 0.028	0.123	0.037
[0.2, 0.4)	-0.009 ± 0.014	0.476	0.114
[0.4, 0.6)	0.017 ± 0.017	0.855	0.18
[0.6, 1.0)	0.163 ± 0.04	1.651	0.328

Table 3. The $\langle b_y P_e \rangle$ contributed by unbound gas and the prediction from scenario 1 & 2.

In this work, we measure the 1h- and 2h-term simultaneously. These two provide an estimation of the electron pressure of gas bounded to the halo $\langle b_y P_e \rangle_{\text{bound}}$ and the total electron pressure $\langle b_y P_e \rangle$ in the universe separately. Therefore, there is a chance to measure the electron pressure contributed by unbound gas.

$$\langle b_y P_e \rangle_{\text{unbound}} = \langle b_y P_e \rangle^{2h} - \langle b_y P_e \rangle_{\text{bound}}^{1h}. \quad (39)$$

The $\langle b_y P_e \rangle_{\text{unbound}}$ in different redshift bins are shown in Table.3. In redshift bin $0 \leq z < 0.2$ and $0.6 \leq z < 1$, a none-zero $\langle b_y P_e \rangle_{\text{unbound}}$ is detected with the measurement significance more than 4σ .

We caution that the above detection are still preliminary and further investigations are needed to verify it. Nevertheless, this exercise points out the stacking tSZ measurement is a promising probe of the thermal energy by these diffuse gas out of the halo. For these reasons we present two scenarios and compare them with the measurement. In scenario 1, We assume the unbound gas would accumulate around the halo and not lose thermal energy when escaping the halo. So the b_y and P_e of these unbound gas is rough similar with those bound to halos. Then,

$$\langle b_y P_e \rangle_{\text{unbound}}^{s1} = \int \frac{\Omega_b / \Omega_m - f_{\text{gas}}}{f_{\text{gas}}} \frac{d \langle b_y P_e \rangle_{\text{bound}}}{d \lg M} d \lg M. \quad (40)$$

In scenario 2, we assume the unbound gas would not relate to their original host halos any more and follow the distribution of dark matter with $b_y = 1$, while the temperature of them is still the same with the bound ones. In this case,

$$\langle b_y P_e \rangle_{\text{unbound}}^{s2} = \int \frac{\Omega_b / \Omega_m - f_{\text{gas}}}{f_{\text{gas}}} \frac{d \langle P_e \rangle_{\text{bound}}}{d \lg M} d \lg M. \quad (41)$$

$\langle b_y P_e \rangle$ of these scenarios are summarized in the third and fourth columns of Table.3. The value of scenarios 1 is more than 10 times

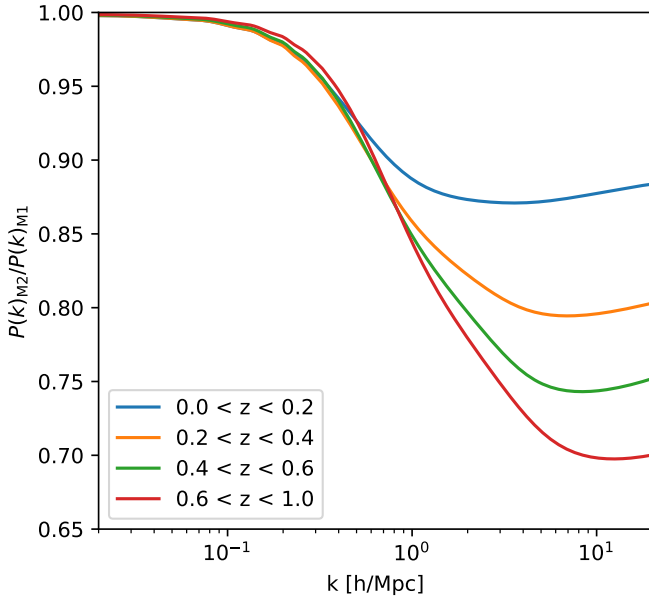


Figure 9. The estimated suppression of matter power spectrum due to the loss of baryons in clusters/groups. The solid lines are the ratio of matter power spectrum of model 2 (with baryon feedback) and model 1 (without baryon feedback) in four redshift bins.

larger than the measurement. This means both P_e and b_y for unbound gas should be much smaller than the bound. And the unbound gas should reside far away from the halo. In addition, for scenario 2 the prediction is 2-3 times larger than the measurement. From this, it can be inferred that the temperature of the gas would decrease largely when they escape the halo.

5.3 The suppression of weak lensing power spectrum

The above results lead to an important conclusion on the weak lensing power spectrum. We utilize the measurement in Sec.5.1 and adopt the halo model from (Mead et al. 2020). Here is a brief description of the halo model to estimate the lensing statistics. The total power spectrum is the sum of a 1h- and 2h-term

$$P_{2h,\mu\nu}(k) = P_{\text{lin}} \prod_{i=\mu,\nu} \left[\int b(M) W_i(M, z) n(M) dM \right] \quad (42)$$

$$P_{1h,\mu\nu}(k) = \int W_\mu(M, z) W_\nu(M, z) n(M) dM, \quad (43)$$

where P_{lin} is the linear matter power spectrum, $b(M)$ is the linear halo bias, $n(M)$ is the halo mass function, and μ, ν represent different matter components such as dark matter, bound gas, and unbound gas. For dark matter, we adopt the 'NFW' profile

$$\rho_{\text{DM}} \propto \frac{1}{r/r_s(1+r/r_s)^2} \quad (44)$$

(Navarro et al. 1997). For gas, we adopt a KS profile (Komatsu & Seljak 2001). The normalization of these profiles is determined by

$$f_i(M)M = \int_0^{r_\nu} 4\pi r^2 \rho_i(M, r) dr. \quad (45)$$

f_{dm} equals to $(\Omega_m - \Omega_b)/\Omega_m$. For gas, we set two models to characterize the impact of baryon feedback. For model 1, $f_{\text{bound}} = \Omega_b/\Omega_m$

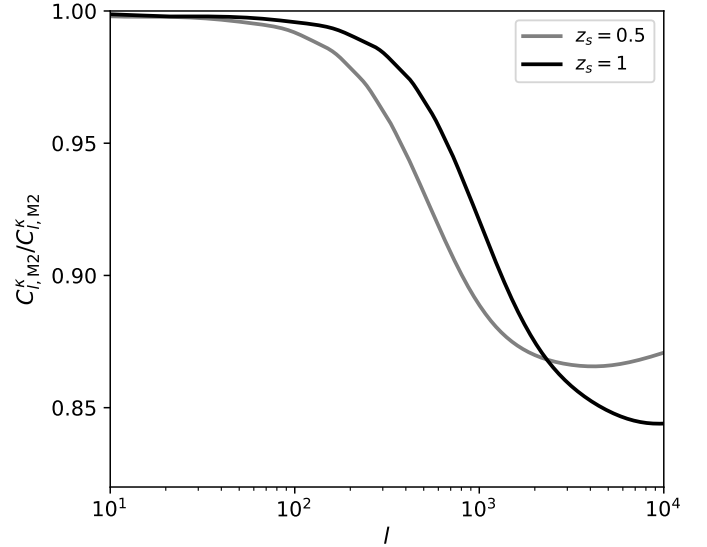


Figure 10. The estimated suppression of the weak lensing power spectrum due to loss of baryons in clusters/groups. The lensed source is at $z_s = 0.5$ (grey) and $z_s = 1$ (black).

and $f_{\text{unbound}} = 0$ which is without baryon feedback. And for model 2, $f_{\text{bound}} = f_{\text{gas}}$ measured in Sec.5.1 as a function of mass and redshift and $f_{\text{unbound}} = \Omega_b/\Omega_m - f_{\text{gas}}$. We adopt the approximation that the unbound gas does not contribute to the 1h-term, but only to 2h-term.

We show the ratio of matter power spectrum of model 2 and model 1 in Fig.9. This ratio quantifies the impact of feedback. At $k = 1\text{Mpc}/h$, the matter spectrum is suppressed 10% at $z=0$ and increasing to 20% at $z=1$. The suppression at smaller scales is larger.

We also show the suppression on weak lensing angular power spectrum, when the source is at $z_s = 0.5$ or $z_s = 1$ in Fig.10. The suppression is about $\gtrsim 10\%$ when $l \gtrsim 1000$. This suppression is an order of magnitude larger than the precision of the weak lensing measurement by Stage IV. This indicates the baryon feedback effect needs to be taken into account in weak lensing measurement. Otherwise, it would become a serious systematic entering cosmology constraint from weak lensing measurement with the stage IV survey, such as EUCLID (Laureijs et al. 2011), LSST (LSST Science Collaboration et al. 2009) and WFIRST (Spergel et al. 2015).

Nowadays, a large set of hydrodynamic simulations are used to characterize the suppression of matter power spectrum caused by baryon and its feedback effects (Semboloni et al. 2011; Chisari et al. 2018; Schneider et al. 2019; Debackere et al. 2020). Harnois-Déraps et al. (2015) constructs an analytic fitting formula that describes the effect of the baryons on the mass power spectrum based on three scenarios of the OWL simulations. Giri & Schneider (2021) finds the suppression reaches a maximum of 20-28 percent at around $k \sim 7h/\text{Mpc}$ and produces an emulator of baryonic effects on the matter power spectrum. van Daalen et al. (2020) utilizes a set of 92 matter power spectra from several hydrodynamic simulations to conduct a detailed investigation of the dependence on different ΛCDM cosmologies, neutrino masses, subgrid prescriptions, and AGN feedback strengths. And they find effectiveness of AGN feed-

back significantly influence the matter power spectrum on the scale scales $k > 0.1h/\text{Mpc}$. And, in this work, we provide an estimation on how the baryon feedback in the Universe would influence the matter power spectrum and weak lensing measurements from tSZ effect observation.

6 DISCUSSION AND CONCLUSION

In this work, we utilize the Yang et al. (2021) cluster sample from DESI group catalog DR9 and *Planck* MILCA y-map to measure the tSZ signal. With 0.8 million galaxy clusters/groups and reasonable mass estimation and completeness, we are able to measure both 1h-term and 2h-term with high S/N. The 1h-term measurement provides a differential description of the cluster/group thermal energy, while the 2h-term provides an integral constraint on the thermal energy of all hot baryons, bound and unbound. The 1h-term measurements extend the $Y - M$ relation by one order of magnitude in the mass range. We further find the sign of departure in the $Y - M$ redshift evolution from the prediction of adiabatic gas physics. The 2h-term measurements are consistent with previous works, but with smaller errorbars. The comparison between 1h- and 2h-terms provides clue to unbound gas and the impact of feedback. An important cosmological implication is the significant suppression of the weak lensing auto power spectrum which is $\gtrsim 10\%$ at $l \gtrsim 1000$. This confirms the baryonic effect as a major systematic in weak lensing.

Although the total S/N of the tSZ detection exceeds 70, our measurement and theoretical interpretation suffer from a number of uncertainties. It is beyond the scope of this work to fully account for these uncertainties in the analysis, due to complexities in describing them and incapability of constraining them by the data. Instead, we list the major uncertainties and discuss the improvements that will be achieved by upcoming surveys.

(a) Redshift uncertainty. The redshift of clusters in DESI group catalog DR9 is photometric and its uncertainty is about $0.01(1+z)$ (Yang et al. 2021). The uncertainty of redshift would cause mistuning clusters in different redshift bins and result in biased templates of 1h- and 2h-term, especially in low redshift bins. The ongoing DESI spectroscopic survey will directly provide spectroscopic redshifts for a fraction of member galaxies. For the rest, cross-correlation between the groups and spectroscopic galaxies will tightly constrain mean redshift of group samples and possibly the outlier rate.

(b) Mass uncertainty. The mass uncertainty for DESI group catalog DR9 is 0.2 dex at the high-mass-end and 0.45 dex at the low-mass-end. In Appendix.A, we use mock data from the simulation to calibrate the mass of clusters in the catalog. However, the number of halos in the simulation is limited, which would cause uncertainty on the $\lg M_t - \lg M_L$ relation. Furthermore, the halo mass function in the simulation relies on the reference cosmology. This may induce certain model dependence in the measurements. The mass uncertainty can be calibrated against cross-correlation with cosmic shear (e.g the catalog⁴ constructed by the Fourier-Quad method (Zhang 2008)) or spectroscopic galaxies.

(c) The halo concentration. In Sec.3, we assume the concentration of halo is the same as the dark-matter-only situation. However, if a large fraction of baryon is blown away from a halo, the halo would become less compact, corresponding to a smaller concentration.

Then the 1h-term profile would be changed. In appendix.B, we test how the change of concentration would influence our results. Fortunately, we find the influence can't be distinguished within the errorbar, largely due to the poor *Planck* angular resolution. On the other hand, it means the current data are not accurate enough to constrain the halo concentration. Stacking cosmic shear around these groups will constrain not only the total mass but also the concentration-mass relation⁵.

(d) Mis-centering. To account for mis-centering of clusters, we set $\eta_{\text{mc}} = 0.2$ in Eq.12 for our fiducial measurement. In appendix.C, we discuss how the parameter η_{mc} would influence the results and find $\eta_{\text{mc}} = 0.2$ is an optimal choice. Further analysis may adopt more complicated and more realistic description of mis-centering (e.g Yan et al. (2020)). With higher resolution CMB experiments such as ACT, SPT, and CMB-S4, the tSZ data alone will have constraining power for both c and the mis-centering effect.

(e) Residual foregrounds in tSZ map. This work adopts *Planck* y-map. In the future, we may follow Chiang et al. (2020) to include non-*Planck* measurements in infrared bands and construct better cleaned y-maps.

7 ACKNOWLEDGMENTS

This work is supported by the national science foundation of China (Nos. 11621303, 11833005, 11890692), National key R&D Program of China (Grant No. 2020YFC2201602), CSST CMS-CSST-2021-A02, 111 project No. B20019, and Shanghai Natural Science Foundation, grant Nos. 15ZR1446700 and 19ZR1466800.

This work made use of the Gravity Supercomputer at the Department of Astronomy, Shanghai Jiao Tong University.

Softwares: astropy (Astropy Collaboration et al. 2013), numpy (Harris et al. 2020), matplotlib (Hunter 2007), scipy (Virtanen et al. 2020), hmf (Murray 2014), healpy (Zonca et al. 2019)

DATA AVAILABILITY

The data underlying this article will be shared on reasonable request to the corresponding author.

REFERENCES

- Amodeo, S., Battaglia, N., Schaan, E., et al. 2021, Phys. Rev. D, 103, 063514, doi: [10.1103/PhysRevD.103.063514](https://doi.org/10.1103/PhysRevD.103.063514)
- Astropy Collaboration, Robitaille, T. P., Tollerud, E. J., et al. 2013, A&A, 558, A33, doi: [10.1051/0004-6361/201322068](https://doi.org/10.1051/0004-6361/201322068)
- Bleem, L. E., Stalder, B., de Haan, T., et al. 2015, ApJS, 216, 27, doi: [10.1088/0067-0049/216/2/27](https://doi.org/10.1088/0067-0049/216/2/27)
- Bolliet, B., Comis, B., Komatsu, E., & Macías-Pérez, J. F. 2018, MNRAS, 477, 4957, doi: [10.1093/mnras/sty823](https://doi.org/10.1093/mnras/sty823)
- Brodwin, M., Greer, C. H., Leitch, E. M., et al. 2015, ApJ, 806, 26, doi: [10.1088/0004-637X/806/1/26](https://doi.org/10.1088/0004-637X/806/1/26)
- Carlstrom, J. E., Holder, G. P., & Reese, E. D. 2002, ARA&A, 40, 643, doi: [10.1146/annurev.astro.40.060401.093803](https://doi.org/10.1146/annurev.astro.40.060401.093803)
- Chiang, Y.-K., Makiya, R., Ménard, B., & Komatsu, E. 2020, ApJ, 902, 56, doi: [10.3847/1538-4357/abb403](https://doi.org/10.3847/1538-4357/abb403)

⁴ <https://gax.sjtu.edu.cn/data/DESI.html>

⁵ Private communication with Jiaqi Wang, Jun Zhang and Xiaohu Yang on their ongoing work of group-shear cross-correlation

- Chisari, N. E., Richardson, M. L. A., Devriendt, J., et al. 2018, MNRAS, 480, 3962, doi: [10.1093/mnras/sty2093](https://doi.org/10.1093/mnras/sty2093)
- de Graaff, A., Cai, Y.-C., Heymans, C., & Peacock, J. A. 2019, A&A, 624, A48, doi: [10.1051/0004-6361/201935159](https://doi.org/10.1051/0004-6361/201935159)
- Debackere, S. N. B., Schaye, J., & Hoekstra, H. 2020, MNRAS, 492, 2285, doi: [10.1093/mnras/stz3446](https://doi.org/10.1093/mnras/stz3446)
- Duffy, A. R., Schaye, J., Kay, S. T., & Dalla Vecchia, C. 2008, MNRAS, 390, L64, doi: [10.1111/j.1745-3933.2008.00537.x](https://doi.org/10.1111/j.1745-3933.2008.00537.x)
- Fukugita, M., & Peebles, P. J. E. 2004, ApJ, 616, 643, doi: [10.1086/425155](https://doi.org/10.1086/425155)
- Gatti, M., Pandey, S., Baxter, E., et al. 2021, arXiv e-prints, arXiv:2108.01600. <https://arxiv.org/abs/2108.01600>
- Giri, S. K., & Schneider, A. 2021, J. Cosmology Astropart. Phys., 2021, 046, doi: [10.1088/1475-7516/2021/12/046](https://doi.org/10.1088/1475-7516/2021/12/046)
- Gonzalez, A. H., Sivanandam, S., Zabludoff, A. I., & Zaritsky, D. 2013, ApJ, 778, 14, doi: [10.1088/0004-637X/778/1/14](https://doi.org/10.1088/0004-637X/778/1/14)
- Gouin, C., Gallo, S., & Aghanim, N. 2022, arXiv e-prints, arXiv:2201.00593. <https://arxiv.org/abs/2201.00593>
- Harnois-Déraps, J., van Waerbeke, L., Viola, M., & Heymans, C. 2015, MNRAS, 450, 1212, doi: [10.1093/mnras/stv646](https://doi.org/10.1093/mnras/stv646)
- Harris, C. R., Millman, K. J., van der Walt, S. J., et al. 2020, Nature, 585, 357, doi: [10.1038/s41586-020-2649-2](https://doi.org/10.1038/s41586-020-2649-2)
- Hasselfield, M., Hilton, M., Marriage, T. A., et al. 2013, J. Cosmology Astropart. Phys., 2013, 008, doi: [10.1088/1475-7516/2013/07/008](https://doi.org/10.1088/1475-7516/2013/07/008)
- Hernández-Monteagudo, C., Trac, H., Verde, L., & Jimenez, R. 2006, ApJ, 652, L1, doi: [10.1086/510123](https://doi.org/10.1086/510123)
- Hill, J. C., Baxter, E. J., Lidz, A., Greco, J. P., & Jain, B. 2018, Phys. Rev. D, 97, 083501, doi: [10.1103/PhysRevD.97.083501](https://doi.org/10.1103/PhysRevD.97.083501)
- Hojjati, A., McCarthy, I. G., Harnois-Déraps, J., et al. 2015, J. Cosmology Astropart. Phys., 2015, 047, doi: [10.1088/1475-7516/2015/10/047](https://doi.org/10.1088/1475-7516/2015/10/047)
- Hojjati, A., Tröster, T., Harnois-Déraps, J., et al. 2017, MNRAS, 471, 1565, doi: [10.1093/mnras/stx1659](https://doi.org/10.1093/mnras/stx1659)
- Horowitz, B., & Seljak, U. 2017, MNRAS, 469, 394, doi: [10.1093/mnras/stx766](https://doi.org/10.1093/mnras/stx766)
- Hunter, J. D. 2007, Computing in Science and Engineering, 9, 90, doi: [10.1109/MCSE.2007.55](https://doi.org/10.1109/MCSE.2007.55)
- Hurier, G., Aghanim, N., Douspis, M., & Pointecouteau, E. 2014, A&A, 561, A143, doi: [10.1051/0004-6361/201322632](https://doi.org/10.1051/0004-6361/201322632)
- Kim, J., Golwala, S., Bartlett, J. G., et al. 2021, arXiv e-prints, arXiv:2110.15381. <https://arxiv.org/abs/2110.15381>
- Kitayama, T. 2014, Progress of Theoretical and Experimental Physics, 2014, 06B111, doi: [10.1093/ptep/ptu055](https://doi.org/10.1093/ptep/ptu055)
- Komatsu, E., & Seljak, U. 2001, MNRAS, 327, 1353, doi: [10.1046/j.1365-8711.2001.04838.x](https://doi.org/10.1046/j.1365-8711.2001.04838.x)
- . 2002, MNRAS, 336, 1256, doi: [10.1046/j.1365-8711.2002.05889.x](https://doi.org/10.1046/j.1365-8711.2002.05889.x)
- Koukoufilippas, N., Alonso, D., Bilicki, M., & Peacock, J. A. 2020, MNRAS, 491, 5464, doi: [10.1093/mnras/stz3351](https://doi.org/10.1093/mnras/stz3351)
- Laureijs, R., Amiaux, J., Arduini, S., et al. 2011, arXiv e-prints, arXiv:1110.3193. <https://arxiv.org/abs/1110.3193>
- Le Brun, A. M. C., McCarthy, I. G., & Melin, J.-B. 2015, MNRAS, 451, 3868, doi: [10.1093/mnras/stv1172](https://doi.org/10.1093/mnras/stv1172)
- Lim, S. H., Mo, H. J., Li, R., et al. 2018, ApJ, 854, 181, doi: [10.3847/1538-4357/aaa21](https://doi.org/10.3847/1538-4357/aaa21)
- Lim, S. H., Mo, H. J., Lu, Y., Wang, H., & Yang, X. 2017, MNRAS, 470, 2982, doi: [10.1093/mnras/stx1462](https://doi.org/10.1093/mnras/stx1462)
- Lim, S. H., Mo, H. J., Wang, H., & Yang, X. 2020, ApJ, 889, 48, doi: [10.3847/1538-4357/ab63df](https://doi.org/10.3847/1538-4357/ab63df)
- LSST Science Collaboration, Abell, P. A., Allison, J., et al. 2009, arXiv e-prints, arXiv:0912.0201. <https://arxiv.org/abs/0912.0201>
- Ma, Y.-Z., Gong, Y., Tröster, T., & Van Waerbeke, L. 2021, MNRAS, 500, 1806, doi: [10.1093/mnras/staa3369](https://doi.org/10.1093/mnras/staa3369)
- Ma, Y.-Z., Van Waerbeke, L., Hinshaw, G., et al. 2015, J. Cosmology Astropart. Phys., 2015, 046, doi: [10.1088/1475-7516/2015/09/046](https://doi.org/10.1088/1475-7516/2015/09/046)
- Marriage, T. A., Acquaviva, V., Ade, P. A. R., et al. 2011, ApJ, 737, 61, doi: [10.1088/0004-637X/737/2/61](https://doi.org/10.1088/0004-637X/737/2/61)
- Mead, A. J., Tröster, T., Heymans, C., Van Waerbeke, L., & McCarthy, I. G. 2020, A&A, 641, A130, doi: [10.1051/0004-6361/202038308](https://doi.org/10.1051/0004-6361/202038308)
- Meinke, J., Böckmann, K., Cohen, S., et al. 2021, ApJ, 913, 88, doi: [10.3847/1538-4357/abf2b4](https://doi.org/10.3847/1538-4357/abf2b4)
- Muñoz, J. B., & Loeb, A. 2018, Phys. Rev. D, 98, 103518, doi: [10.1103/PhysRevD.98.103518](https://doi.org/10.1103/PhysRevD.98.103518)
- Murray, S. 2014, HMF: Halo Mass Function calculator. <http://ascl.net/1412.006>
- Navarro, J. F., Frenk, C. S., & White, S. D. M. 1997, ApJ, 490, 493, doi: [10.1086/304888](https://doi.org/10.1086/304888)
- Osato, K., Shirasaki, M., Miyatake, H., et al. 2020, MNRAS, 492, 4780, doi: [10.1093/mnras/staa117](https://doi.org/10.1093/mnras/staa117)
- Pandey, S., Baxter, E. J., & Hill, J. C. 2020, Phys. Rev. D, 101, 043525, doi: [10.1103/PhysRevD.101.043525](https://doi.org/10.1103/PhysRevD.101.043525)
- Pandey, S., Gatti, M., Baxter, E., et al. 2021, arXiv e-prints, arXiv:2108.01601. <https://arxiv.org/abs/2108.01601>
- Planck Collaboration, Ade, P. A. R., Aghanim, N., et al. 2014a, A&A, 571, A29, doi: [10.1051/0004-6361/201321523](https://doi.org/10.1051/0004-6361/201321523)
- . 2014b, A&A, 571, A20, doi: [10.1051/0004-6361/201321521](https://doi.org/10.1051/0004-6361/201321521)
- . 2015, A&A, 581, A14, doi: [10.1051/0004-6361/201525787](https://doi.org/10.1051/0004-6361/201525787)
- Planck Collaboration, Aghanim, N., Arnaud, M., et al. 2016, A&A, 594, A22, doi: [10.1051/0004-6361/201525826](https://doi.org/10.1051/0004-6361/201525826)
- Planck Collaboration, Aghanim, N., Akrami, Y., et al. 2020, A&A, 641, A6, doi: [10.1051/0004-6361/201833910](https://doi.org/10.1051/0004-6361/201833910)
- Reichardt, C. L., Stalder, B., Bleem, L. E., et al. 2013, ApJ, 763, 127, doi: [10.1088/0004-637X/763/2/127](https://doi.org/10.1088/0004-637X/763/2/127)
- Ruppin, F., Mayet, F., Pratt, G. W., et al. 2018, A&A, 615, A112, doi: [10.1051/0004-6361/201732558](https://doi.org/10.1051/0004-6361/201732558)
- Schneider, A., & Teyssier, R. 2015, J. Cosmology Astropart. Phys., 2015, 049, doi: [10.1088/1475-7516/2015/12/049](https://doi.org/10.1088/1475-7516/2015/12/049)
- Schneider, A., Teyssier, R., Stadel, J., et al. 2019, J. Cosmology Astropart. Phys., 2019, 020, doi: [10.1088/1475-7516/2019/03/020](https://doi.org/10.1088/1475-7516/2019/03/020)
- Semboloni, E., Hoekstra, H., Schaye, J., van Daalen, M. P., & McCarthy, I. G. 2011, MNRAS, 417, 2020, doi: [10.1111/j.1365-2966.2011.19385.x](https://doi.org/10.1111/j.1365-2966.2011.19385.x)
- Shao, J., Zhang, P., Lin, W., & Jing, Y. 2011, ApJ, 730, 127, doi: [10.1088/0004-637X/730/2/127](https://doi.org/10.1088/0004-637X/730/2/127)
- Sheth, R. K., Mo, H. J., & Tormen, G. 2001, MNRAS, 323, 1, doi: [10.1046/j.1365-8711.2001.04006.x](https://doi.org/10.1046/j.1365-8711.2001.04006.x)
- Spacek, A., Richardson, M. L. A., Scannapieco, E., et al. 2018, ApJ, 865, 109, doi: [10.3847/1538-4357/aada01](https://doi.org/10.3847/1538-4357/aada01)
- Spergel, D., Gehrels, N., Baltay, C., et al. 2015, arXiv e-prints, arXiv:1503.03757. <https://arxiv.org/abs/1503.03757>
- Sun, M., Voit, G. M., Donahue, M., et al. 2009, ApJ, 693, 1142, doi: [10.1088/0004-637X/693/2/1142](https://doi.org/10.1088/0004-637X/693/2/1142)
- Sunyaev, R. A., & Zeldovich, Y. B. 1972, Comments on Astrophysics and Space Physics, 4, 173
- Tanimura, H., Hinshaw, G., McCarthy, I. G., et al. 2019, MNRAS, 483, 223, doi: [10.1093/mnras/sty3118](https://doi.org/10.1093/mnras/sty3118)
- Tröster, T., Mead, A. J., Heymans, C., et al. 2021, arXiv e-prints, arXiv:2109.04458. <https://arxiv.org/abs/2109.04458>
- van Daalen, M. P., McCarthy, I. G., & Schaye, J. 2020, MNRAS, 491, 2424, doi: [10.1093/mnras/stz3199](https://doi.org/10.1093/mnras/stz3199)
- Van Waerbeke, L., Hinshaw, G., & Murray, N. 2014, Phys. Rev. D, 89, 023508, doi: [10.1103/PhysRevD.89.023508](https://doi.org/10.1103/PhysRevD.89.023508)
- Vikhlinin, A., Burenin, R. A., Ebeling, H., et al. 2009, ApJ, 692, 1033, doi: [10.1088/0004-637X/692/2/1033](https://doi.org/10.1088/0004-637X/692/2/1033)
- Vikram, V., Lidz, A., & Jain, B. 2017, MNRAS, 467, 2315, doi: [10.1093/mnras/stw3311](https://doi.org/10.1093/mnras/stw3311)
- Virtanen, P., Gommers, R., Oliphant, T. E., et al. 2020, Nature Methods, 17, 261, doi: [10.1038/s41592-019-0686-2](https://doi.org/10.1038/s41592-019-0686-2)
- Yan, Z., Raza, N., Van Waerbeke, L., et al. 2020, MNRAS, 493, 1120, doi: [10.1093/mnras/staa295](https://doi.org/10.1093/mnras/staa295)
- Yan, Z., van Waerbeke, L., Tröster, T., et al. 2021, A&A, 651, A76, doi: [10.1051/0004-6361/202140568](https://doi.org/10.1051/0004-6361/202140568)
- Yang, X., Mo, H. J., van den Bosch, F. C., & Jing, Y. P. 2005, MNRAS, 356, 1293, doi: [10.1111/j.1365-2966.2005.08560.x](https://doi.org/10.1111/j.1365-2966.2005.08560.x)
- Yang, X., Mo, H. J., van den Bosch, F. C., et al. 2007, ApJ, 671, 153, doi: [10.1086/522027](https://doi.org/10.1086/522027)
- Yang, X., Xu, H., He, M., et al. 2021, ApJ, 909, 143, doi: [10.3847/1538-4357/abddb2](https://doi.org/10.3847/1538-4357/abddb2)

- Zhang, J. 2008, MNRAS, 383, 113, doi: [10.1111/j.1365-2966.2007.12585.x](https://doi.org/10.1111/j.1365-2966.2007.12585.x)
- Zhang, P., & Pen, U.-L. 2001, ApJ, 549, 18, doi: [10.1086/319067](https://doi.org/10.1086/319067)
- Zhang, P., Pen, U.-L., & Trac, H. 2004, MNRAS, 355, 451, doi: [10.1111/j.1365-2966.2004.08328.x](https://doi.org/10.1111/j.1365-2966.2004.08328.x)
- Zhao, D. H., Jing, Y. P., Mo, H. J., & Börner, G. 2009, ApJ, 707, 354, doi: [10.1088/0004-637X/707/1/354](https://doi.org/10.1088/0004-637X/707/1/354)
- Zonca, A., Singer, L., Lenz, D., et al. 2019, The Journal of Open Source Software, 4, 1298, doi: [10.21105/joss.01298](https://doi.org/10.21105/joss.01298)

APPENDIX A: THE RELATIONSHIP BETWEEN THE TRUE MASS AND THE OBSERVED MASS

In DESI group catalog DR9, the assigned halo mass M_L and halo true mass M_t is not a one-to-one relation. In Fig.A1, we show the difference $\delta \lg M$ of $\lg M_L$ and $\lg M_t$ and its scatter $\sigma_{\lg M}$. The mean value and the scatter are all dependent on $\lg M_L$. The amplitude of 1h-term is proportional to $M^{5/3}$. Thus the uncertainty of 0.2 dex for mass means 2.2 times difference for the 1h-term profile. Therefore it is necessary to calibrate the cluster mass when calculating the 1h-term template. Otherwise the measurement f_{gas} would be catastrophically biased. We show how to obtain an appropriate 1h-term profile according to the $\lg M_t - \lg M_L$ distribution relation as follows.

Using these mock data, we can obtain the possibility distribution of $\delta \lg M$ in the mass bin $\lg M_1 < \lg M < \lg M_2$. Fig.A2 shows the PDF and CDF of $\delta \lg M$ in four redshift bins. Then the 1h-profile of an observed cluster sample is

$$y_\theta = \int_{z_{\min}}^{z_{\max}} \int_{\lg M_{L,\min}}^{\lg M_{L,\max}} \int_{\lg M_t=0}^{\lg M_t=\infty} y_\theta(\lg M_t, z) n(\lg M_t, z) p(\delta \lg M = \lg M_t - \lg M_L | \lg M_L) d \lg M_t d \lg M_L dz, \quad (\text{A1})$$

$y_\theta(\lg M_t, z)$ is the y-profile of a halo whose mass and redshift are M_t and z , $n(\lg M_t, z)$ is the number of clusters in the mass bin $(\lg M_t - \frac{d \lg M_t}{2}, \lg M_t + \frac{d \lg M_t}{2})$ and redshift bin $(z - \frac{dz}{2}, z + \frac{dz}{2})$, and $p(\delta \lg M | \lg M_L)$ is the PDF of $\delta \lg M$ at $\lg M_L$. When the bin length $d \lg M_L$ and dz small enough, Eq.A1 is the unbiased 1h-term template for the cluster sample with $z_{\max} < z < z_{\min}$ and $\lg M_{L,\max} < \lg M_L < \lg M_{L,\min}$.

Here we do not consider the uncertainty of the PDF $p(\delta \lg M | \lg M_L)$. However, the number of halos is decreasing with the halo mass, so there are only a few massive halos in massive mass bins. This may cause a large uncertainty on the estimate of the mean value of $\delta \lg M$ and the total PDF at large $\lg M_t$. Therefore we abandon the most massive bin in redshift $0.2 < z < 0.4$ and $0.4 < z < 0.6$, whose $M_L \geq 10^{14.9} M_\odot/h$, in fitting relation of f_{gas} and halo mass M .

APPENDIX B: CONCENTRATION

In the fiducial measurement, we assume the concentration-mass relation from (Duffy et al. 2008) for dark matter halos. However, the effects from baryon would influence the concentration and the 1h-term profile. In Section.5.1, it has been observe more than a half of baryon is blown away from the halo with $M < 10^{14} M_\odot/h$. Therefore, these halos would become more incompact. Follow (Mead et al. 2020), we adopt the method to modify the concentration by

unbound gas

$$c_{\text{new}}(M) = c(M) \left[1 + \eta_c \left(1 - \frac{f_{\text{gas}}}{\Omega_b / \Omega_m} \right) \right]. \quad (\text{B1})$$

When $f_{\text{gas}} = 0$, $c_{\text{new}}(M) = c(M)$ the same as the fiducial case. And when all of the baryon is blown away from the halo, $f_{\text{gas}} = 1$, $c_{\text{new}}(M) = (1 + \eta_c)c(M)$. The factor $1 + \eta_c$ can characterize how the concentration of a halo would change, if it lose all baryons. Here, we compare three situation with $\eta_c = 0, -0.1, -0.2$. In Fig.B1, we show the comparison of these three situations for four redshift bins. For each redshift bin, the top panel shows the ratio of the fitted f_{gas} and the fiducial case. The bottom panel shows the ratio of χ_{\min}^2 and the fiducial case.

For massive, low-redshift cluster samples, the fitted f_{gas} increases with the decreasing of η_c . For other cluster bins, the fitted f_{gas} decreases with the decreasing of η_c . And the low-mass clusters are more sensitive to the modification of concentration because their baryon abundance is lower. However, the measurement uncertainties of the low-mass cluster sample are also larger.

Fortunately, all differences cannot be distinguished by the $1-\sigma$ errorbar. Therefore, the simple fiducial assumption of concentration would not bias the measurements. On the other hand, this means our measurement cannot raise a constraint on the halo concentration currently.

APPENDIX C: MIS-CENTERING

In DESI group catalog DR9, the position of clusters would have misalignments with the actual minimum gravitational potential points of them. This mis-centering would suppress stacked tSZ profiles. Here, we treat this effect as the same way of the beam in the CMB survey when generating 1h- and 2h-term templates. We assume the amplitude of the mis-centering is proportional to the virial radius of a halo.

$$\sigma_{\text{mc}} = \eta_{\text{mc}} \frac{r_v}{d_c} \quad (\text{C1})$$

And in the templates of 1h- and 2h-term, the parameter σ_{beam} is replaced by $\sigma_{\text{eff}} = \sqrt{\sigma_{\text{beam}}^2 + \sigma_{\text{mc}}^2}$.

In Fig.C1, we test how the parameter η_{mc} would influence the measurements. In the top panel of each redshift, it shows the ratio of the f_{gas} with $\eta_{\text{mc}} = 0, 0.1, 0.2, 0.3, 0.4$ and case with $\eta_{\text{mc}} = 0$. And the bottom panels show the ratio of χ_{\min}^2 .

We find the η_{mc} indeed have a large influence on the fitting, especially for the low redshift, massive cluster samples. For small clusters and high redshift clusters, the σ_{mc} is smaller than the beam size σ_{beam} , due to small r_v or large d_c . In this situation, the fitting is less sensitive to the mis-centering effect. Low-redshift samples suffer from mis-centering effect more seriously. For most cluster samples with $0 \leq z < 0.2$, when $\eta_{\text{mc}} = 0.2$, χ_{\min}^2 reaches the minimum point. Therefore, we set $\eta_{\text{mc}} = 0.2$ in the fiducial measurement.

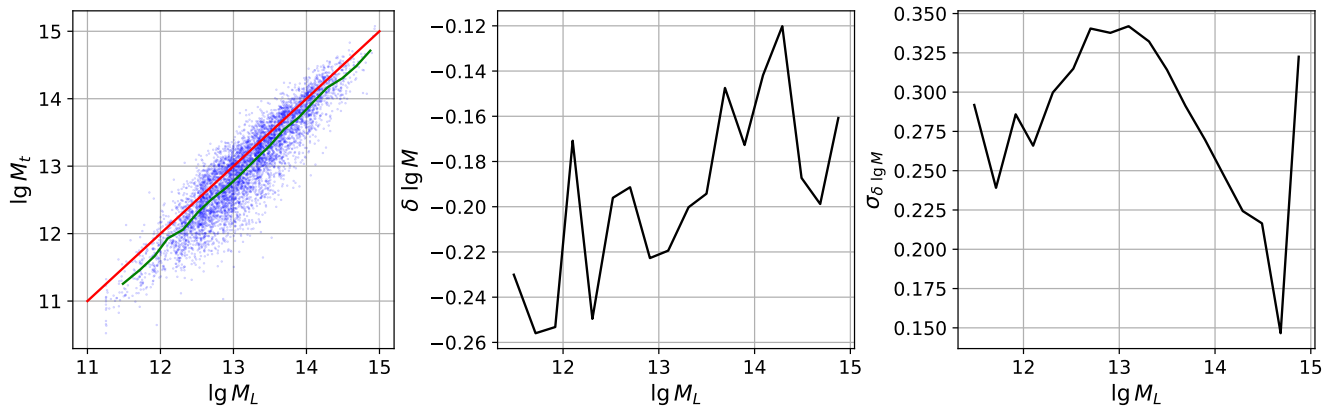


Figure A1. **Left:** each blue point represents a halo in the Mock catalog, the x- and y-axis is the assigned mass and the true mass. Red line is $y = x$ and green is the mean $\lg M_t$ as a function of $\lg M_L$. **Middle:** The mean value of the difference $\delta \lg M$ as a function of $\lg M_L$. **Right:** The scatter of the difference $\delta \lg M$ as a function of $\lg M_L$.

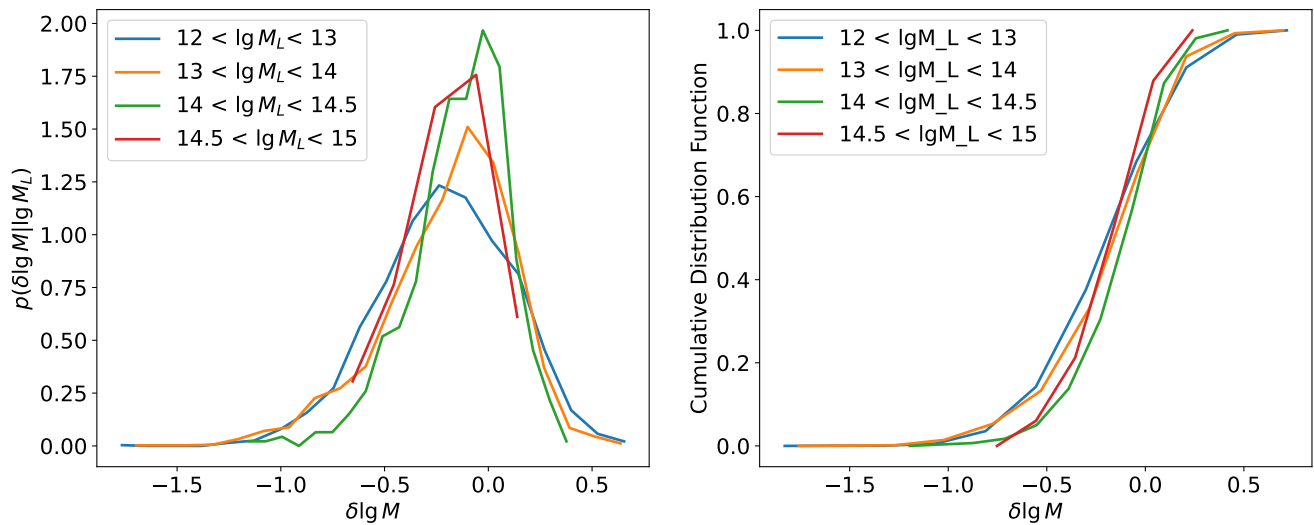


Figure A2. The PDF (left) and CDF (right) of $\delta \lg M$ as a function of $\lg M_L$ in different redshift bins. In the mass bin $14.5 < \lg M_L < 15$, the number of cluster in the mock catalog is too less to construct a precise description of the PDF. This may induce bias into 1h-term template estimation.

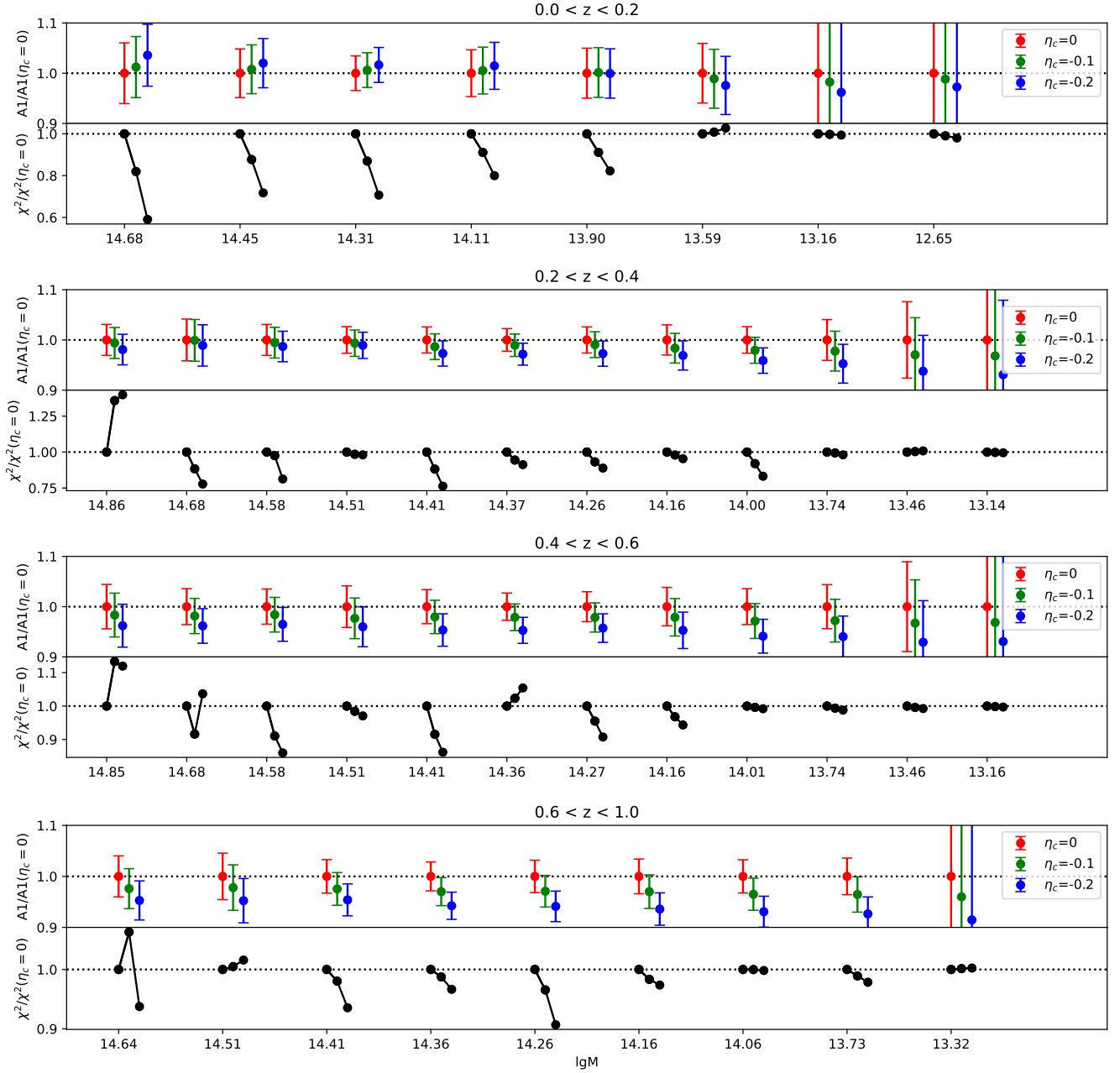


Figure B1. The coefficient of the 1h-term influenced by concentration model. The three different concentration models are $\eta_c = 0, -0.1, -0.2$ represented by red, green and blue points. η_c is the parameter that characterizes how the concentration is sensitive to the fraction of baryon in a halo (Eq.B1). The redshift bin is the label on the top of each panel. The top part of each panel shows A_1 of each mass bin for the three models. And to make the figure more readable, each point is normalized by the $A_1(\eta_c = 0)$ in the same bin. The bottom part shows the χ^2_{\min} .

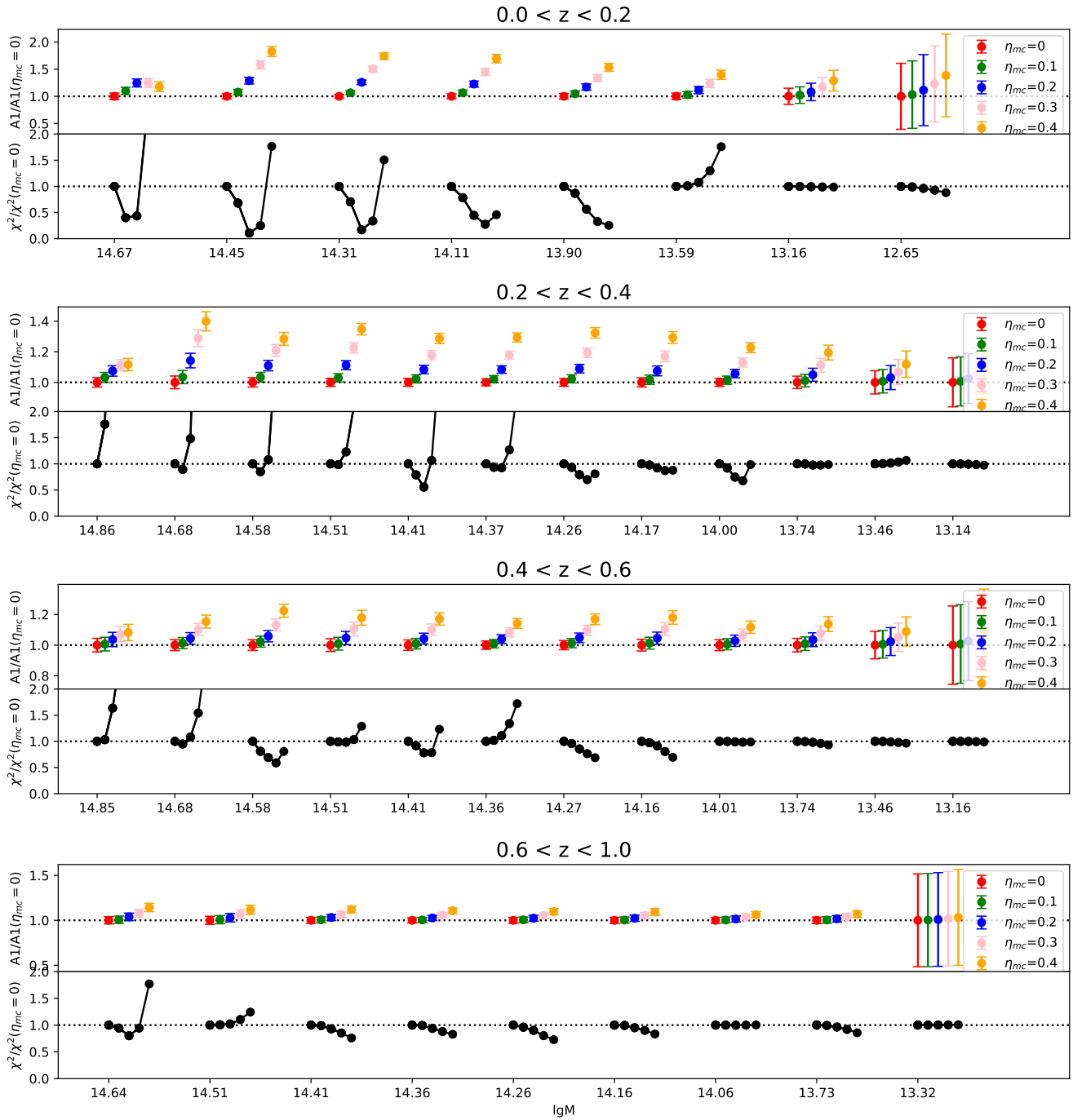


Figure C1. The same with Fig.B1 but for different mis-centering models with $\eta_{mc} = 0, 0.1, 0.2, 0.3, 0.4$.